

Signature of supervisor



Universiteit
Antwerpen



TECHNISCHE
UNIVERSITÄT
WIEN
Vienna University of Technology

Masterthesis

Evaluation of the log ratio method as an alternative for quantitative micro x-ray fluorescence scanning measurements

carried out at the

Department of Chemistry

of the University of Antwerp

Supervisors

Prof. Dr. Piet Van Espen (University of Antwerp)

Ao. Univ. Prof. Dr. Gernot Friedbacher (Vienna University of Technology)

by

Martin Miedler, BSc

Kegelgasse 16/1/1, 1030 Vienna, Austria

“A common mistake that people make when trying to design something completely foolproof is to underestimate the ingenuity of complete fools.”

Douglas Adams – The Hitchhikers Guide to the Galaxy

Acknowledgment

I would like to thank my supervisor at the Vienna University of Technology, Prof. Dr. Gernot Friedbacher for his assistance prior to my Erasmus stay and for his valuable support and guidance during the final phase of my thesis.

Special thanks are directed towards my supervisor at the University of Antwerp, Prof. Dr. Piet van Espen for giving me the opportunity to work in his laboratory during my Erasmus stay.

I would also like to thank all my colleagues and friends in Antwerp for making my Erasmus stay a unique experience.

Last but not least, thanks to my family and friends for their support during the course of my degree and this thesis.

STATUTORY DECLARATION

I declare that I have authored this thesis independently, that I have not used other than the declared sources / resources and that I have explicitly marked all material which has been quoted either literally or by content from the used sources.

Vienna, February 9, 2015

Ort, Datum

Martin Miedler

Abstract

Energy-dispersive XRF analysis provides a fast, non-destructive way to determine element distributions of samples. Once a calibration is done, the method provides an almost effortless way to achieve quantitative information. However, these calibrations are most often not linear and do not pass the origin thus they are only applicable in a very narrow range around the used standards. With the 2008 presented log-ratio calibration equation (LRCE) a promising method that aimed to get rid of this non-linearity has been introduced.

The current work investigates how well the method achieves this goal by measuring a set of seven standards with a micro-focused XRF setup and a commercially available hand-held XRF device from Bruker. Parameters goodness-of-fit R^2 , slope α and y-intercept β have been calculated and compared with both XRF devices as well as the Compton peak correction and the raw data set.

Prior to the micro XRF measurements the setup had to be rebuild due to a relocation, thus requiring a check of the system performance. This was done by a long-term drift measurement, ensuring that the same results are achieved in every measurement.

Apart from these calibrations, measurements with the hand-held device have been carried out in the historic japanese tower in Brussels.

The drift measurements pointed out a slight drift for high count rate elements but the error could be rendered insignificant when correction methods are applied. The calculations of the micro XRF setup reveals that the LRCE correction is favorable to the Compton peak correction. The performance is especially good for poorly correlated elements. For the hand-held device only elements with low signal and strong air absorption perform better with the LRCE. The measurements of the historic site in Brussels could identify some of the applied materials an techniques on paper and wood basis.

Contents

Introduction	13
Aim of this work	14
I Theory	15
1 X-ray fluorescence spectrometry	16
1.1 Excitation sources	16
1.2 Wavelength dispersive spectrometer	18
1.3 Energy dispersive spectrometer	19
1.4 Microbeam XRF	22
1.5 Spectrum artifacts	25
2 Interaction of x-ray photons with matter	26
2.1 Photoelectric absorption	28
2.2 Auger effect and fluorescence yield	29
2.3 Compton scattering	31
2.4 Rayleigh scattering	32
II Instrumentation	34
3 Micro XRF setup	35
3.1 Parameters	37
4 Hand-held XRF	38
4.1 Parameters	38
5 Software	40
5.1 bAxil	40
5.1.1 Evaluation of the recorded spectra with bAxil	41
5.2 Matlab	44
6 United States geological survey standards	45

III	Methods	47
7	Quantitative analysis of samples by XRF	48
7.1	The fundamental parameter relation	48
8	Calibration and correction procedures	52
8.1	Estimation of the regression parameters	52
8.2	General calibration equation in XRF analysis	53
8.3	Straight line regression analysis and calibration	55
8.4	The Compton corrected matrix effect	57
8.5	Compositional data	58
8.6	Elemental ratios	61
8.7	The log-ratio calibration equation	63
IV	Results and discussion	65
9	Micro XRF setup	66
9.1	Drift measurements	66
9.2	Line scans	69
9.3	Comparison of calibration methods	70
9.4	Geological sample	74
10	Hand-held XRF	79
10.1	Comparison of calibration methods	79
10.2	Japanese tower in Brussels	82
11	Conclusions	92
	Bibliography	97
	Appendix	98

Introduction

In 1895 the German physicist Conrad Röntgen accidentally discovered the x-rays subsequently named after him. He was working with an cardboard covered, electrical discharge tube, when he noticed a shimmer on a nearby barium platinocyanide painted cardboard [1]. After the wave nature of x-rays was proven in 1912 by Laue, Friedrich and Knipping (by diffracting x-rays with a coppersulfat pentahydrate crystal), the importance of x-rays for analytical chemistry could be shown by Henry G. J. Moseley. He observed, that the characteristic wavelength of the x-rays corresponded to the atomic number in the anodes of the discharge-tubes he used. He furnished evidence, that the atomic numbers were based on a physical measurable variable [2].

The first prototype of a wavelength-dispersive x-ray fluorescence (XRF) spectrometer was built by Friedman and Birks in 1948 [3]. The detectable elements reached already a remarkable range from Beryllium to Uranium. Twentythree years later, the first energy-dispersive systems using Si(Li) detectors were developed at the Lawrence Berkeley National Laboratories.

Early XRF spectrometers were originally regarded as quantitative analytical instruments, due to their well defined measurement geometry under laboratory conditions. Soon after, the introduction of smaller, mobile XRF spectrometers induced a shift from purely laboratory use and to in-field experiments. This change of environment presented quantitative analysis with a problem. The measurement geometry was no longer defined, owing to varying distances and angles between sample and excitation source (and sample and detector respectively), inhomogeneous composition and uneven (e.g. curved) sample surfaces. The challenge is to turn the information retrieved under difficult analytical circumstances into useful data for the user.

During Apollo 15 and 16, an XRF spectrometer was carried in the Command Service Module. The device measured the characteristic x-rays of the lunar surface produced by the solar x-rays. An interesting detail of this experiment is, that the researchers used ratios instead of absolute concentrations to present their data. *Clark and Hawke* for example mapped the Si/Mg distribution on the lunar surface with concentration ratios (see figure 1) [4].

Element-ratios also found to be useful in geology, since a lot of times

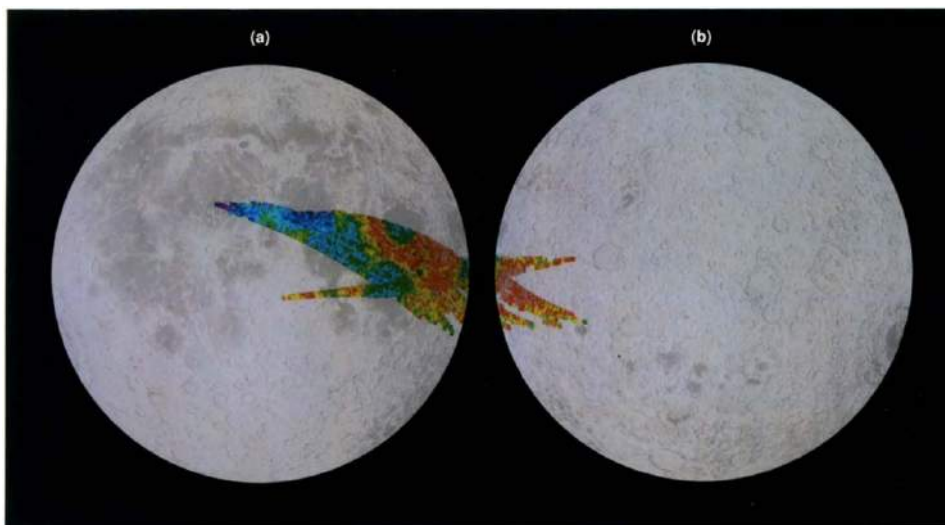


Figure 1: A map of the lunar surface, using Mg/Si concentration ratios, obtained from the orbital x-ray measurements on the Apollo 15 and 16 missions. The colors refer to the different Mg/Si element ratios: pink, > 0.31 ; red, $0.28-0.31$; yellow, $0.26-0.28$; green, $0.25-0.26$; cyan, $0.24-0.25$; blue, $0.23-0.24$; violet, < 0.23 (after Clark and Hawke, 1981 in [4])

the focus lies on comparing and correlating geological samples, rather than determining the actual composition. Element ratios have been successfully applied to e.g. bore-cores from palaeoceanographic environments [5–7].

Aim of this work

The current work takes a closer look at more recent developments in the evaluation and calibration of geological samples. A new calibration procedure has been proposed by *Weltje et al.* [7, 8]. This method uses logarithmic ratios of element intensities rather than plain element intensities.

To evaluate this method, USGS¹ standards were prepared and measured with two different devices, a micro XRF setup in the lab and a commercially available hand-held device. Prior to the micro XRF measurements, the setup had to be rebuilt and validated due to a relocation. The prepared standards had to be verified as well.

During my work with the hand-held XRF device, Prof. Dr. Koen Janssens offered me the opportunity to carry out measurements in the Japanese tower in the royal gardens in Brussels. The work in Brussels did not match the goal of this thesis, but due to the historic value of the location I didn't want to decline.

¹abbr.: *United States Geological Survey*

Part I
Theory

Chapter 1

X-ray fluorescence spectrometry

This introductory chapter deals with x-ray fluorescence spectrometry as an analytical technique, giving an overview on the working principle of different builds and their components.

From all analytical techniques available, x-ray fluorescence (XRF) is the only one, which is capable of detecting all major and minor elements (from Be - U), while requiring only minimal or no sample preparation. Every XRF spectrometer, no matter which design, contains at least the following three components:

- An excitation source (either a x-ray tube or radio isotopes)
- A sample holder
- A spectrometer (wavelength or energy dispersive)

In addition, a suitable data collection and processing system is necessary.

1.1 Excitation sources

The excitation sources can be divided into:

X-ray tubes produce x-rays by accelerating thermal electrons from a tungsten filament towards an anode due to a high positive voltage relative to the cathode (up to 40 kV). A Wehnelt cylinder, biased several hundred volts negative compared to the filament, focuses the electrons by applying a repulsive electrostatic field [9]. When the electrons hit the anode, they are decelerated by collisions with the target atoms, producing a continuum, the bremsstrahlung and the characteristic x-rays (see also section 2.3 on page 31). The current in the filament determines the amount of electrons and thus radiation is produced, while

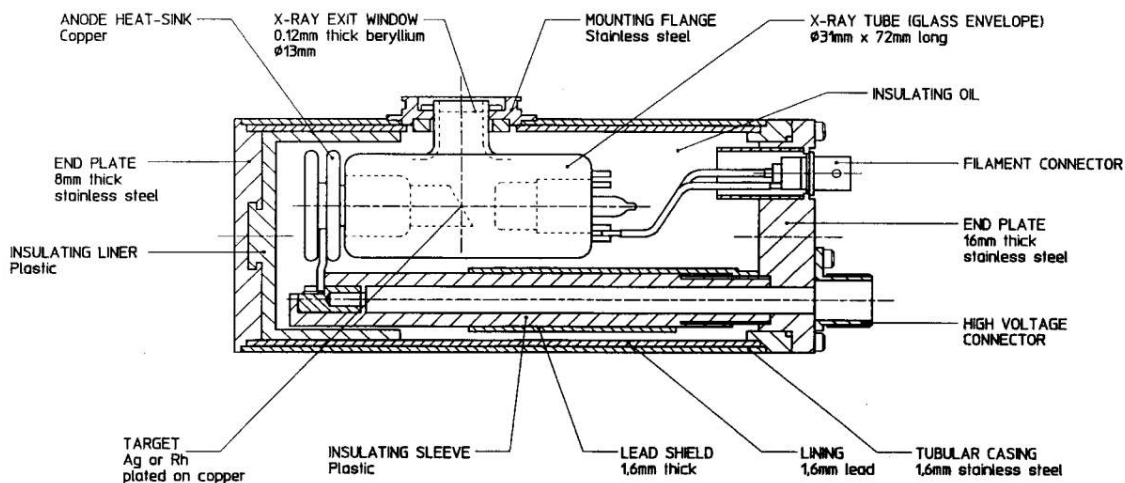


Figure 1.1: Schematic drawing of a side window tube. The actual x-ray tube is vacuumed, made of glass and contains the W-filament with the Wehnelt cylinder and the target (very pure Cr, Mo, Rh, Ag or W) (after R. Van Grieken in [9]).

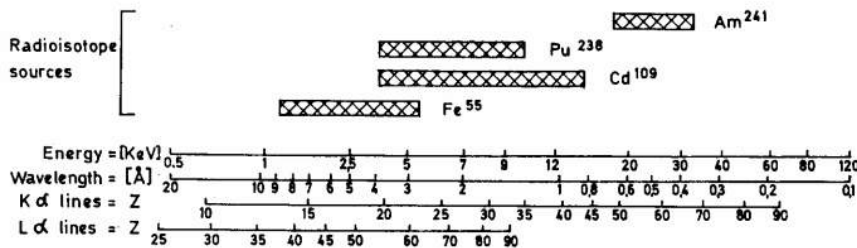


Figure 1.2: Excitation ranges of commonly used radioisotopes (adapted from Bertin, 1975 in [10])

the voltage applied to the anode defines the energy of the radiation. Two designs are common, the side window tube (see figure 1.1) and the front window tube.

Radio isotopes are used in cases where highly monochromatic radiation without continuum is required, or in cases where no energy and only limited space is available (e.g. hand-held devices). When e.g. ^{55}Fe (26 protons and 30 neutrons) captures a K -shell electron, a proton and the electron form a neutron, resulting in ^{55}Mn (25 protons and 30 neutrons) with a K -shell vacancy. Through photoelectric absorption (see section 2.1, page 28), it comes eventually to the emission of Mn K_{α} and Mn K_{β} radiation.

XRF spectrometers most commonly divided based on their design:

1.2 Wavelength dispersive spectrometer

Wavelength dispersive (WD) spectrometers are based on the principle of Bragg diffraction. The characteristic x-rays are diffracted according to their wavelength on a crystal (e.g. LiF). For an integer number of the wavelength difference $n\lambda$, the Bragg condition is fulfilled and the constructive interference allows the detector to measure the intensity of the specific wavelength.

$$2d \sin \theta = n\lambda \quad \text{with } n = 1, 2, \dots \quad (1.1)$$

The crystal in the center of the goniometer turns about θ , while the detector moves around the crystal in intervals of 2θ , measuring all wavelengths and their intensities sequentially. The primary x-rays are aligned with a collimator. This system requires a complex mechanical design, but allows an excellent energy resolution of 10 - 20 eV (FWHM¹) without peak overlaps. The major disadvantage is the long measuring time (circa 30 min per sample) and their bulkiness. For routine measurements of very few defined elements, WD XRF is with about 15 000 units still most prevalent.

Equipped with a flow proportional counter and a scintillation detector, wavelength dispersive spectrometers are able to measure all elements between Be and U.

Flow proportional counters are either flooded with Ar (+10 % CH₄) or He (+12 % CO₂) and covers the longer wavelengths $>2 \text{ \AA}$ ($<7 \text{ keV}$). It has a metal wire in the middle, which has a positive high voltage of 1 - 3 kV. It attracts the electrons created during the ionization process of the gas atoms, as they are hit by x-rays. On their way to the cathode they are accelerated and create an avalanche of new ion/electron pairs, resulting eventually in the creation of a current pulse in the wire.

Scintillation detectors have a thallium-doped sodium iodide [NaI(Tl)] crystal, that triggers a light pulse caused by the incoming x-rays. The intensity of the emitted pulse is proportional to the number of electrons excited by the incoming x-rays. The light pulse is absorbed by the photocathode, which releases photoelectrons as a consequence. The electrons are multiplied in the (vacuumed) photomultiplier and detected as a current pulse in the anode. An Al mirror prevents light from hitting the crystal and makes the detector susceptible only for higher energy photons $>6 \text{ keV}$ ($<2 \text{ \AA}$).

A comparison of the properties of wavelength and energy dispersive spectrometers is given in table 1.1.

¹abbr.: *Full Width Half Maximum*, determines the broadness of the peak at 50 % of the peak maximum.

Table 1.1: Comparison of wavelength and energy dispersive spectrometer (adapted from Margu and R. Van Grieken in [11])

Property	WD XRF	ED XRF
Resolution	very good	lower
Detection	sequential	simultaneously
Detecting efficiency	low	high
Mechanical design	complex	simple
Electronics	simple	complex
Elemental range	Be - U	Be - U [12]
Cost	rel. expensive	rel. inexpensive

1.3 Energy dispersive spectrometer

Compared to wavelength dispersive (WD) spectrometers energy dispersive (ED) spectrometers (see figure 1.3) have a significantly lower resolution of 130 - 200 eV (FWHM). Their big advantage though is the capability of being able to measure all elements from Be to U [12] simultaneously, which greatly reduces the measurement time. This feature is made possible due to the unique properties of silicon in the semiconductor detector (after *Lutz* 1999, p. 79 in [13]):

- The *small band gap* (1.12 eV at room temperature) leads to a large number of charge carriers per unit energy loss of the ionizing particles to be detected. The average energy for creating an electron-hole pair (3.6 eV) is an order of magnitude smaller than the ionization energy of gases.
- The *high density* (2.33 g/cm³) leads to a large energy loss per traversed length of the ionizing particle (3.8 MeV/cm for a minimum ionizing particle). Therefore it is possible to build thin detectors that still produce large enough signals to be measured.
- Electrons and holes can *move almost freely* in the semiconductor. The mobility of electrons ($\mu_p = 1450 \text{ cm}^2/\text{Vs}$) and holes ($\mu_p = 450 \text{ cm}^2/\text{Vs}$) is at room temperature only moderately influenced by doping. Thus charge can be rapidly collected ($\sim 10 \text{ ns}$) and detectors can be used in high-rate environments.
- The *excellent mechanical rigidity* allows the construction of self-supporting structures.

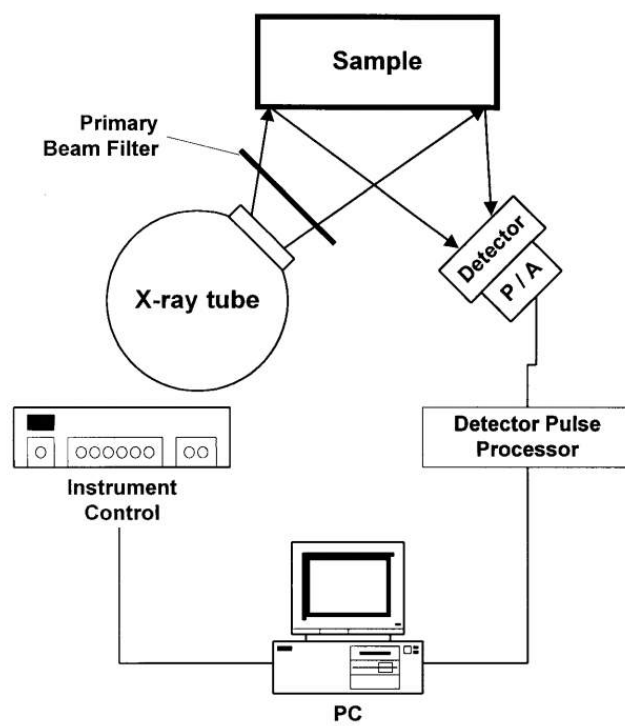


Figure 1.3: *Basic setup of a energy dispersive XRF spectrometer (after R. Van Grieken in [9])*

Two types of semiconductor detectors are common. The lithium-drifted silicon (Si(Li)) detector and the silicon drift detector (SDD):

Si(Li) detectors are semiconductor pin-diodes in form of a lithium-drifted silicon (Si(Li)) crystal. The very pure p -type Si wafer is thereby doped with lithium to compensate for electron holes and achieve an intrinsic region in the middle.

When a reverse (negative) bias is applied, an active depletion region with almost no charge carriers is formed. The remaining current is due to thermal excitation of electrons according to the Boltzmann statistic. To keep the electrons in the valence band and thus avoid leakage current, the detector is permanently cooled with liquid nitrogen (see figure 1.4).

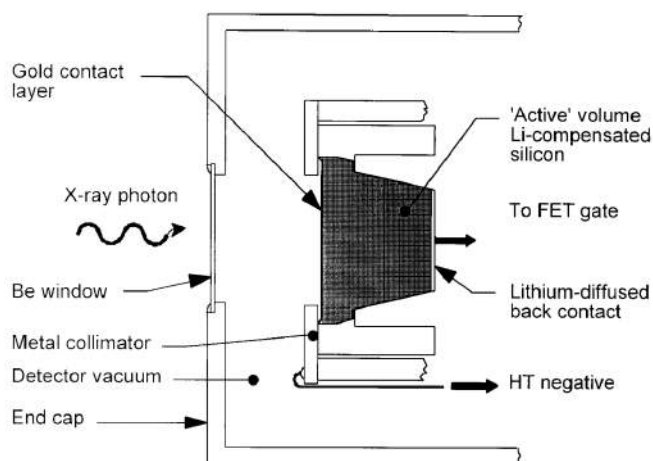


Figure 1.4: Cross section of a $Si(Li)$ detector mounted in its cryostat endcap (after R. Van Grieken in [9]).

As the x-rays reach the intrinsic region in the detector, they create electron-hole pairs through photoelectric absorption (see section 2.1). Through multiple ionization processes, caused by the emission and re-absorption of Auger electrons and low energetic x-rays from the inner-shell vacancy energy, a large number of electrons is produced. The amount of generated electrons depends on the energy of the x-rays. Due to the negative bias (up to -1000 V) on the gold contact layer on the front end of the Si crystal, the electron charge pulse is attracted to the collection plate on the back of the crystal, where a voltage drop is induced. The drop is directly proportional to the amount of electrons and thus to the x-ray energy. Typical dimensions range from $10\text{ - }80\text{ mm}^2$ and a thickness of $3\text{ - }5\text{ mm}$.

Silicon drift detectors (SDD) present the state of the art semiconductor detector technology. The brilliant concept of *E. Gatti and P. Rehak* from 1984 is depicted in figure 1.5 on page 23. They had the idea to measure the position of the electrons by recording the drift time in the detector, whilst the energy of the x-ray is calculated from the charge at the anode. Therefore they placed the *n*-type silicon contact somewhere lateral (figure 1.5 b)) and added another *p*-type contact on the other side. Thereby they created a two side *n*-type silicon contact with the depletion zones facing each other (figure 1.5 c)). As the current is increased, two separated, depleted regions with a conducting undepleted region in between are yielded (figure 1.5 d)). All created electrons assemble in this “potential valley” and traverse the detector only by drifting until they subsequently reach the *n*-electrode. If a current parallel to the surface is added, a *controlled* drift of the electrons is formed.

The sensitivity of an SDD is given through:

$$U_{out} = \frac{Q_{inj}}{C_{tot}} \quad (1.2)$$

with U_{out} the voltage increase that is detected, Q_{inj} the injected charge and C_{tot} the total capacity of the detector. Clearly with decreasing capacity, the sensitivity increases.

In x-ray fluorescence spectroscopy, where no position information is needed, single sided radial electrodes with the anode in the center have been developed [14]. Modern SDDs (see figure 1.6) reach an energy resolution better than 147 eV FWHM (at 5.9 keV, at -10 °C) with a capacitance of ~ 200 fF, latest developments with new layout even better resolutions than 130 eV (at -15 °C, with ~ 120 fF) [15]. A disadvantage is that they have a low efficiency above 10 keV since they are very thin (300 - 500 μm) compared to Si(Li) detectors (3 - 5 mm).

1.4 Microbeam XRF

The microbeam setup (see figure 1.7 on page 24) differs from a standard ED XRF spectrometer in that point, that the primary x-rays, generated in the x-ray tube, impinge *focused* on the sample surface. This is done in the simplest way by means of a focusing capillary (see figure 1.8 on page 24) and a gimbal mechanic, that is mounted in front of the Be window of the x-ray tube. The gimbal is used to align the capillary ideally, to achieve the maximal transition of the x-rays and thus maximum intensity on the sample surface.

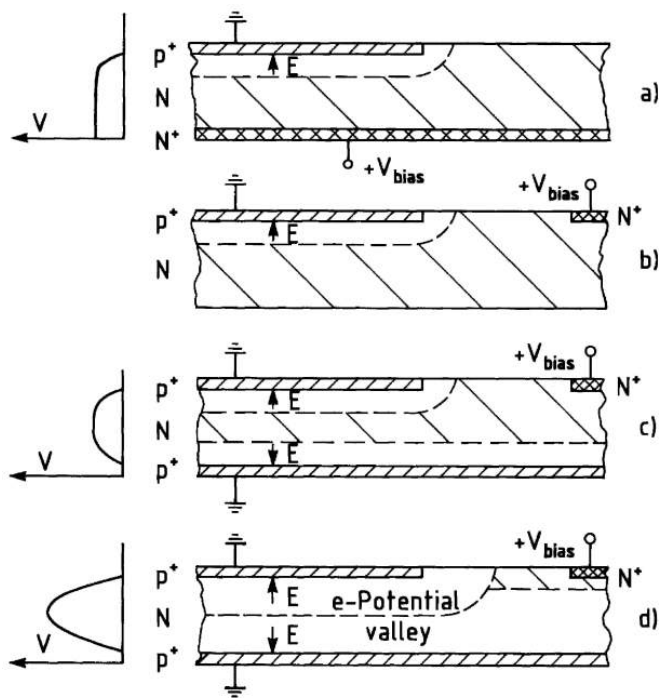


Figure 1.5: Basic ideas that lead to the invention of the drift detector: diode partially depleted (a); diode with depletion from the side (b); double diode partially depleted (c); double diode completely depleted (d) [13].

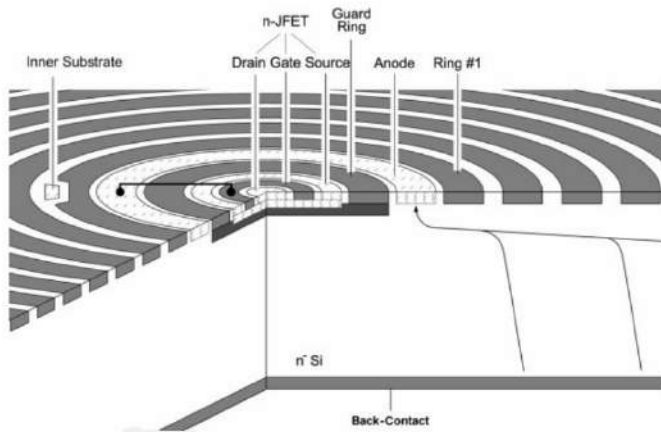


Figure 1.6: Principle of a modern silicon drift detector for XRF spectroscopy. An ionizing particle creates electron-hole pairs along its path through the detector. Electrons drift to the collecting anode, where they create an electric pulse. (after Pahlke et al. 2004, in [15]).

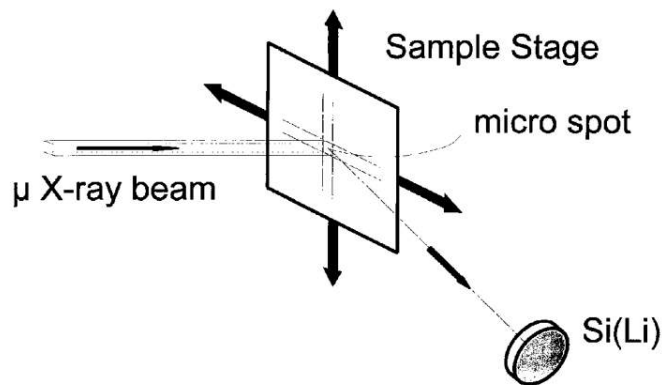


Figure 1.7: Principle of the Microbeam XRF. The focused beam hits the sample, exciting a very small spot. When the sample is placed on the stage, by moving it, a 2D element resolution is yielded [9].

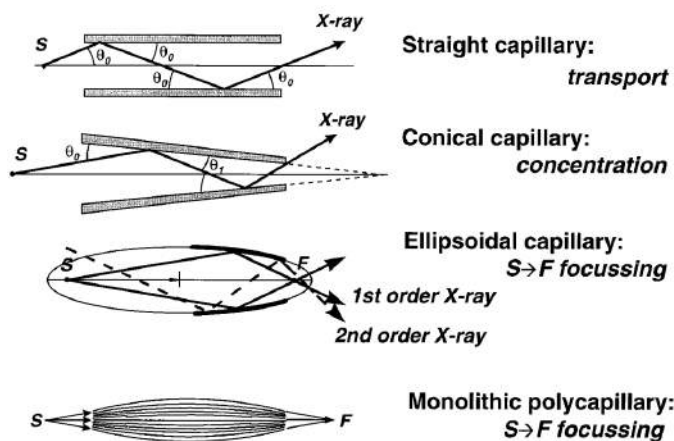


Figure 1.8: X-ray propagation in different capillaries. S denotes the source, F the focus point if existent. Note that only the ellipsoidal and the monolithic polycapillary form a “true” focus point [9].

1.5 Spectrum artifacts

The peaks in an XRF spectra originate largely from the elements in the sample. However, the few peaks that arise due to other sources are called “spectrum artifacts”. The continuum of the x-ray tube and the Compton and Rayleigh peaks are *not* regarded as artifacts. There are two major spectrum artifacts :

Escape peaks emerge when Si K_α -rays, produced by photoelectric absorption, “escape” from the detector during operation. Above the Si K_α absorption edge, incoming x-rays can excite the silicon in the detector (especially at energies close to the absorption edge). Usually, this Si K_α -rays are re-absorbed in the detector bulk and thus contributing to the total charge. Near the surface however, it is possible for the Si K_α -rays to leave the detector, decreasing thereby the number of detected electrons (and subsequently the energy) by this very Si K_α energy: 1.74 keV. The highest probability (close to the absorption edge) for this event is in Si(Li) detectors about 3% [16, 17]. The excitation probability of Si K_β can be ignored completely, the one for Si K_α only above 10 keV.

For high energy photons, Compton escape peaks occur, when a Compton scattered photon leaves the detector. For HPGe detectors, the analogue Ge K_α escape probability is much higher ($\sim 10\%$).

Sum peaks occur when two pulses arrive in such a short time interval, that the pulse processing electronics cannot recognize them as two individual events anymore. A peak with the summarized energy of both pulses is yielded. Sum peaks are easy to identify, since their relative line ratio is not the same as for other energies in the region and they’re only arise for major elements with high count rates. Modern spectrum analyzing softwares are able to correct for these sum peaks.

Apart from those two, *diffraction peaks* can occur when the Bragg condition is met while measuring a crystal sample. The more monochromatic the beam is, the less likely it is. Sometimes it can happen that so called *system contamination peaks* arise. These peaks stem from detector components, e.g. from trace elements in the Be window itself (only visible through total reflection XRF although very unlikely).

Chapter 2

Interaction of x-ray photons with matter

There are two main interactions of photons with matter, which are relevant for XRF analysis:

Absorption of the photon: The absorbed photon disappears, transferring all its energy to the interacting electron, which (if the photon energy is sufficient $E_{\text{Photon}} > E_{\text{Bonding}}$) leaves the ionized atom in form of a photo-electron. The vacancy is filled with an higher shell electron, resulting eventually in the emission of characteristic x-rays or Auger electrons.

Scattering of the photon: The scattering processes build up the continuum observed in a XRF spectra. While a Compton scattered photon transfers its energy partially (depending solely on the incident angle θ) on a weak bound shell-electron ($E_{\text{Photon}} \gg E_{\text{Bonding}}$) and ionizing hence the atom, the frequency of a Rayleigh scattered photon doesn't change, leaving thus the atom unchanged.

The attenuation of the photons depend on the mass absorption coefficient μ (in cm^2/g), the density ρ (in g/cm^3) and the thickness d (in cm) of the material and it is known as Lambert-Beer's law:

$$I = I_0 \cdot e^{-\mu\rho d} \quad (2.1)$$

μ and ρ can be pooled to the linear absorption coefficient $\mu^* = \mu \cdot \rho$.

These independent interactions are expressed as cross sections, which characterize their probability. If all cross sections are added up and normalized to a one atom per square centimeter basis, the total atomic absorption cross section σ_{tot} (in cm^2/Atom) is yielded:

$$\sigma_{tot} = \tau + \sigma_R + \sigma_C + \dots \quad (2.2)$$

where τ is the photo-electric absorption cross section of the K , L and M shell ($\tau = \tau_K + \tau_L + \tau_M$), σ_R the Rayleigh scatter cross section and σ_C the Compton scatter cross section (Klein-Nishina collision cross section [18]). It describes the probability of the photon to have an interaction in the matter of whatsoever kind. It is related to the mass attenuation coefficient by:

$$\mu = \sigma_{tot} \cdot \frac{N_A}{A} \quad (2.3)$$

where A is the atomic weight of a pure material (in kg) and N_A the Avogadro constant ($6.02214078 \cdot 10^{23} \text{ mol}^{-1}$) [19]. If μ is plotted against the photon energy, the characteristic *absorption edges* can be observed (see figure 2.1). The ratio of the mass attenuation coefficient just above and below the absorption edge is called jump ratio.

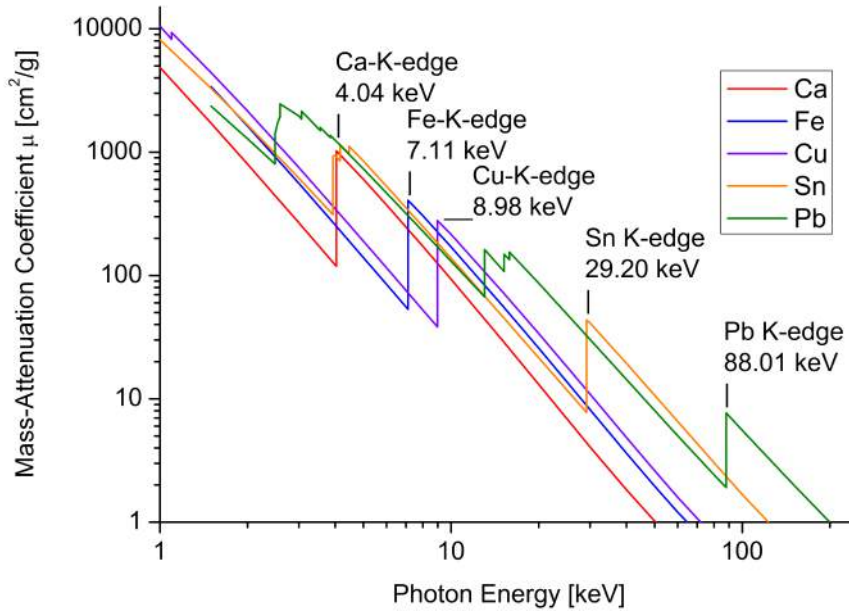


Figure 2.1: When the mass-attenuation coefficient μ is plotted against the photon energy, the characteristic absorption edges can be observed. The K -edge of the shown elements is labeled.

In case of compounds, μ is calculated by summing up the different total cross sections and atomic weights of the components:

$$\mu = \frac{N_A}{\sum_i x_i \cdot A_i} \cdot \sum_i x_i \cdot \sigma_{tot_i} = \sum_{i=1}^n \mu_i \cdot w_i \quad (2.4)$$

where μ_i is the mass attenuation coefficient and w_i is the weight fraction of element i .

2.1 Photoelectric absorption

As mentioned earlier, the photoelectric absorption is responsible for the generation of characteristic x-rays. In detail, an inner shell electron is knocked out of its shell (see figure 2.2). The atom is ionized and goes back into ground state within a few nano seconds, filling the vacancy with an electron from a higher shell. The excess energy between the two shells is emitted in form of an x-ray photon. These (discrete) energies are called *characteristic x-rays*, since they are specific for each element and transition.

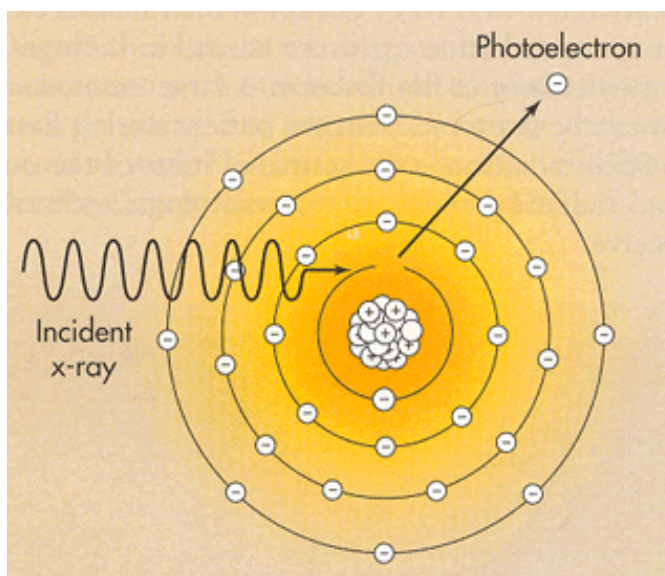


Figure 2.2: High energy photon knocks electron out of inner shell (here: K-shell) during photoelectric absorption [20].

The general relation between wavelength and atomic number is described by Moseley's law [2]:

$$\frac{1}{\lambda} = k \cdot (Z - \sigma)^2 \quad (2.5)$$

According to the Pauli principle, neither two electrons in an atom can have the exact same quantum numbers at the same time and place. They always have to differ in at least one quantum number. The transition to ground state is subject to strict quantum mechanical selection rules (see table 2.1). The change in the principal quantum number n describes the transition from a higher shell into a lower one. The azimuthal quantum number is a measure for the angular momentum in units of \hbar . Since the photon has an angular momentum of \hbar , the angular momentum of the atom has to change by \hbar upon transition in case of absorption or emission to change in order to preserve the angular momentum [21]. The total angular momentum quantum number $j = l + s$ is a combination of the azimuthal

Table 2.1: *Quantum mechanical selection rules*

Quantum number	Rule	Example
principal	$\Delta n = \geq 1$	$L \rightarrow K, M \rightarrow M$
azimuthal	$\Delta l = \pm 1$	$2p \rightarrow 1s, 3p \rightarrow 2p$
tot. angular momentum	$\Delta j = 0, \pm 1$	$3d(j = 2\frac{1}{2}) \rightarrow 2p(j = \frac{1}{2})$

quantum number l and the spin quantum number s . It determines which transitions are allowed [9].

With due regard to these quantum mechanical selection rules, the allowed transitions are listed in table 2.2. Figure 2.3 on page 30 shows an

Table 2.2: *important transitions for XRF analysis*

Transition	Siegbahn Notation	relative Intensity
$L_{3 \rightarrow K}$	$K_{\alpha 1}$	100
$L_{2 \rightarrow K}$	$K_{\alpha 2}$	~ 50
$M_{3,2 \rightarrow K}$	$K_{\beta 1}$	~ 17
$M_{5 \rightarrow K}$	$L_{\alpha 1}$	100
$N_{5,4 \rightarrow K}$	$L_{\beta 2,5}$	~ 25

overview of all the allowed transitions.

2.2 Auger effect and fluorescence yield

Instead of emitting characteristic x-rays after photo absorption, a complementary radiationless mechanism, the Auger effect, can occur. Thereby an electron from a weaker bound shell is released leaving the atom double ionized. The higher the atomic number, the lower is the probability of this effect. A direct consequence is that the actual amount of generated x-rays is lower due to the Auger effect. The K -fluorescence yield is a parameter for the produced x-rays per atom:

$$\omega_K = \frac{I_K}{n_K} \quad (2.6)$$

where I_K is the total number of characteristic K -x-ray photons emitted from the sample and n_K is the number of primary K -shell vacancies [9]. The probability of a radiant transition from the K , L and M shell with the atomic number is given in figure 2.4.

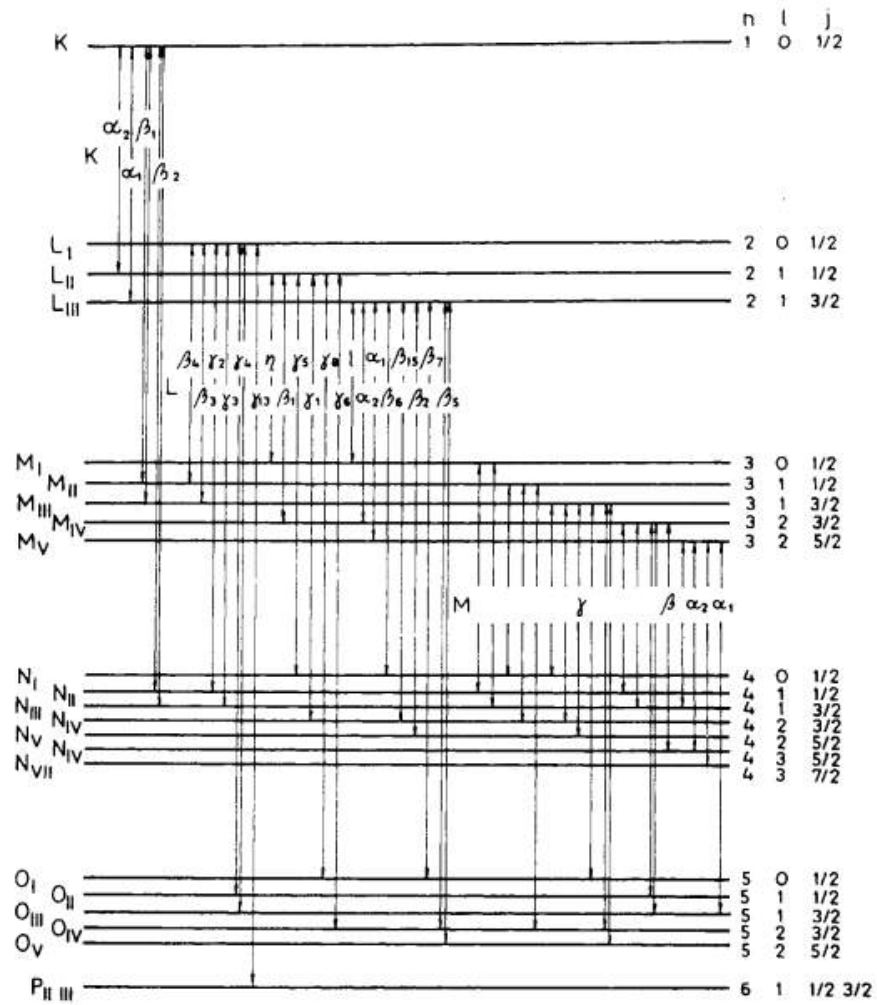


Figure 2.3: Allowed transitions according to the quantum mechanical selection rules including their Siegbahn notation (after Sandström 1957) [22]

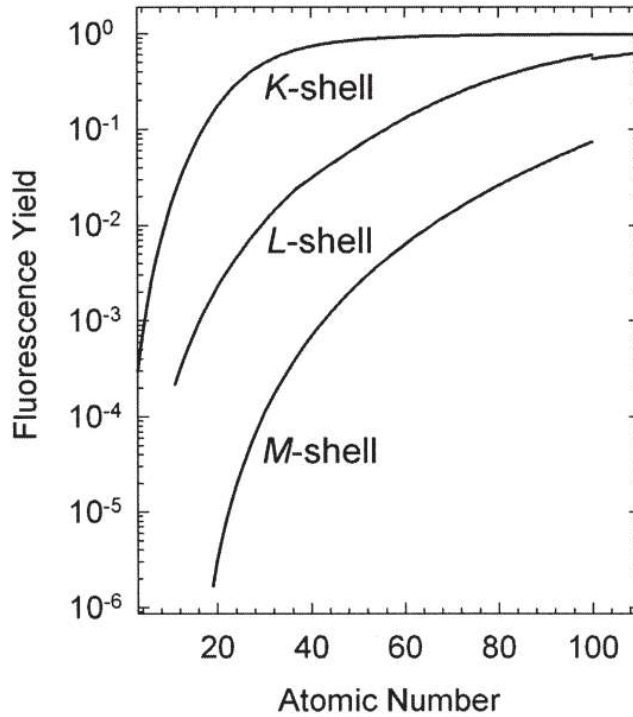


Figure 2.4: Probability of a vacancy being filled by a process causing radiation in competition with the release of an Auger electron. Non-radiative transition dominates only at low atomic numbers, while for high Z elements the emission of characteristic x-rays greatly prevails [23].

2.3 Compton scattering

First conceived by Arthur H. Compton in 1923, the Compton effect describes the inelastic scattering of a photon on a free electron. Despite that, it is commonly used as an approximation for the inelastic interaction of *weakly bound* electrons with photons. It is also a direct proof that light is quantized in form of photons. As the inelastic scatter takes place, part of the photon energy is transferred to the electron, which leaves the atom, while the photon is recoiled with a longer wavelength (see figure 2.5).

Considering the law of conservation of energy

$$\underbrace{h \cdot \nu}_{E_{\text{Photon}}} + \underbrace{m \cdot c^2}_{E_{\text{Electron}}} = \underbrace{h \cdot \nu'}_{E'_{\text{Photon}}} + \underbrace{m \cdot c^2 + p_e \cdot c}_{E'_{\text{Electron}}}$$

and momentum,

$$\vec{p}_{\text{Photon}} = \vec{p}'_{\text{Photon}} + \vec{p}_{\text{Electron}}$$

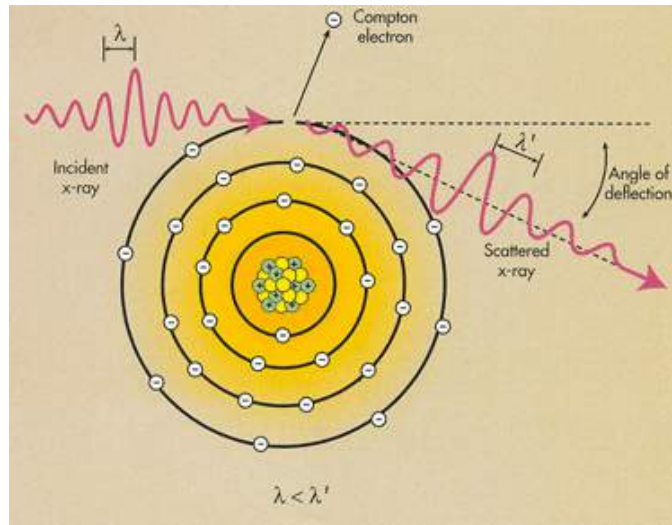


Figure 2.5: During Compton scattering, a high energy photon hits a weakly bound electron and transfers part of its energy to the electron. The electron leaves the atom, while the photon is scattered, having a longer wavelength [20].

the following equation for the wavelength shift can be derived:

$$\lambda' - \lambda = \frac{h}{m_e \cdot c} (1 - \cos \theta) \quad (2.7)$$

where λ respectively λ' is the wavelength before and after scattering, h the Planck constant, m_e the electron rest mass, c the speed of light and θ the scatter angle. The term $\frac{h}{m_e \cdot c}$ is called Compton wavelength ($2.42631021 \dots 10^{-12}$ m [24]). The transfer of energy is zero at $\theta = 0$ (no interaction) and maximal at $\theta = 180$. This distribution can be observed (see figure 2.6, page 33), since with increasing θ the Compton peak (λ') is shifted to longer wavelength (according to equation (2.7)). The second peak (λ) is the Rayleigh scattered peak, which has the same energy as the incident x-rays.

2.4 Rayleigh scattering

Rayleigh scattering occurs during the interaction of a photon with any bound electron of an atom. No energy is transmitted during the process, since the scatter is elastic, thus leaving the atom in its ground state. The wavelength of the scattered x-rays is unchanged and in phase with the other Z electrons of the atom. To calculate the intensity of the scatter radiation, the amplitudes of the scattered x-rays of all the electrons of an atom have to be added up.

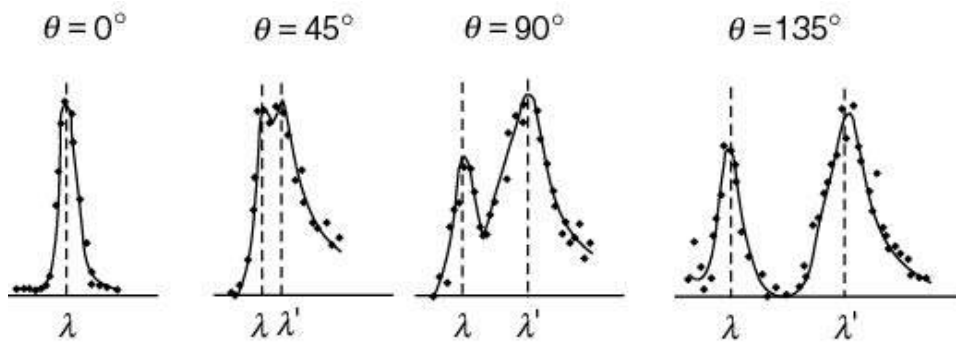


Figure 2.6: Shift of the Compton peak λ' to longer wavelength with scatter angle θ , according to equation (2.7). λ denotes the Rayleigh scatter peak [25].

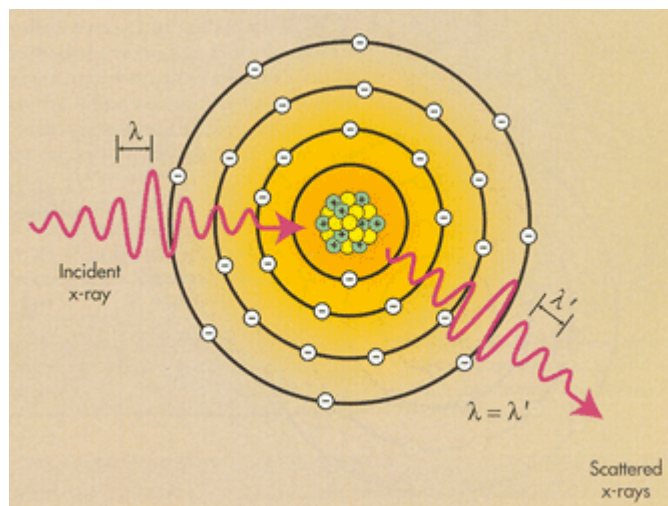


Figure 2.7: During Rayleigh scattering, a photon is elastically scattered on any electron of the atom, without changing its wavelength [20].

Part II

Instrumentation

Chapter 3

Micro XRF setup

This chapter treats the setup and the parameters of the micro-focused XRF spectrometer in the laboratory, that was used to measure the United States geological survey (USGS) standards and the stone sample.

The setup followed the layout that the x-ray tube with the focusing optics is pointing at the sample in an angle of 45° . The detector is mounted 90° to the source (on the same height), focused on the sample spot that is irradiated by the tube. The sample itself was mounted on a stage that could move up and down (remotely controlled) and back and forth (manually controlled). The following devices were used for the setup:

- X-ray source with focusing capillary
- SDD detector
- signal processor
- two sample stages

For the measurements of the *USGS standards* (see figure 3.1), a total of 101 points were measured, with a stepsize of $250\ \mu\text{m}$. The distance between detector and sample was 0.5 cm, the one between sample and detector <1 cm. The spectrum acquisition time was 100 s with an energy of 30 keV and $40\ \mu\text{A}$ in 2048 channels. The deadtime was between 2.8 % (RGM-1) and 5.3 % (BIR-1). The average counts-per-second (CPS) varied depending on the sample between 2050 CPS (RGM-1) and 4000 CPS (BIR-1).

For the measurements of the *rock sample* (see figure 3.2), a total of 161 points were measured, with a stepsize of $500\ \mu\text{m}$. The distance between x-ray source and sample was 1 cm, the distance between sample and detector also 1 cm. The spectrum acquisition time was 60 s with an energy of 30 keV and $40\ \mu\text{A}$ in 2048 channels. The average counts-per-second was around 7500 CPS.

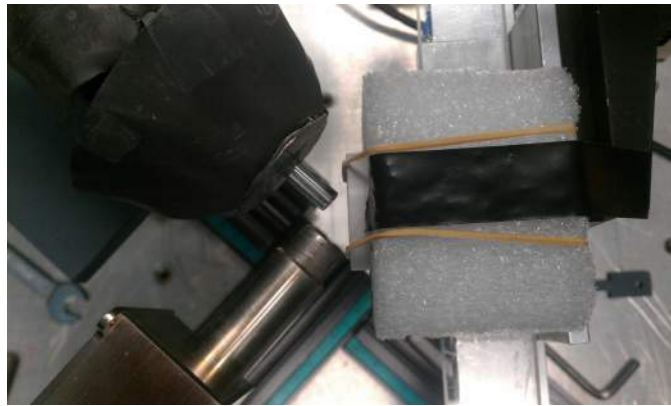


Figure 3.1: *Micro XRF setup for the measurements of the USGS standards. Two simple rubber bands atop a foam cuboid hold the fragile standards in position during the scans.*

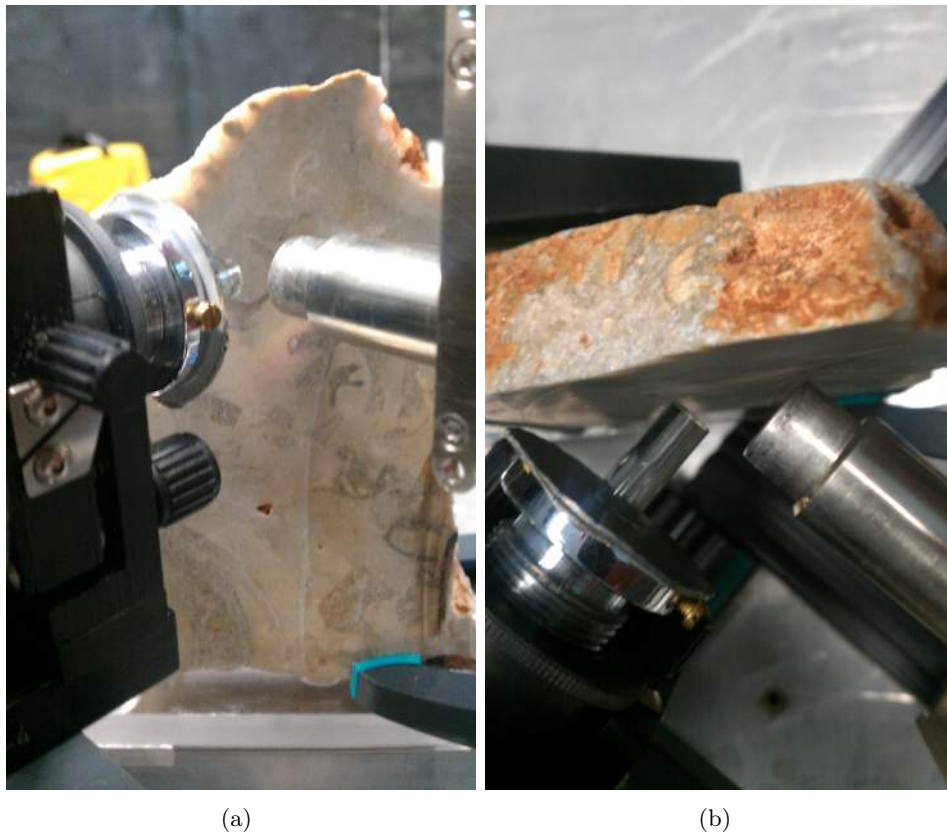


Figure 3.2: *Micro XRF setup for the measurements of the rock sample. The rock was hold in position with a clamp. (a) front view, (b) top view.*

In both cases, the data acquisition was done with the “Newport Canberra controller center”. For the connection and the adjustment of the stepping motors, the program “SMC 100 UserTool” was used. The output files produced can be read using Matlab or processed with the bAxil software.

3.1 Parameters

X-ray source

The following x-ray source was used:

Manufacturer: Moxtex
Name: Magnum
Type: transmission Rh-anode
Power: 10 W (max.)
High voltage: 50 kV (max.)

SDD detector

The following silicon-drift-detector was used:

Manufacturer: Canberra
Name: X-PIPS Detector
Model: SXD 15C – 150 – 500
Serial number: XD145

The specifications according to the data sheet are:

Active area: 15 mm²
Nominal depletion depth: 500 μm

Signal processor

The following digital signal processor was used:

Manufacturer: Canberra
Model: MCA INSPECTOR – 2000

Stage

The following motorized stage was used:

Manufacturer: Newport
Model: SMC 100CC-UTS 100CC

The setup as described above, achieves an energy resolution of 151 eV at 5.89 keV (Mn K_α). The rise time was 5.6 μs with a flat top of 0.8 μs that is equal to a Gaussian shaping time of 2 μs. A throughput of up to 10⁵ CPS without significant spectrum degradation is theoretical possible.

Chapter 4

Hand-held XRF

This chapter describes the hand-held XRF spectrometer from Bruker, that was used during the in-field measurements of the Japanese tower in Brussels.

The measurements that took place in the last week of April 2013, were carried out in the Japanese tower at the royal palace in Brussels. A mobile, hand-held ED XRF spectrometer from Bruker was used. The device was controlled via laptop with a RS-232 to USB cable. The spectrometer was mounted on a tripod to keep it in a fixed position during the measurements.

The data acquisition was done with the software “S1PXRF” from Bruker. For detailed explanation of the procedure of measurement, see Appendix 11. The measurements lasted between 250 and 500 s. In total, 42 different spots were measured including samples of glass, metall, wood and paper. The settings were adjusted in a way that roughly 9 000 - 12 000 cps were reached.

For the data evaluation, the spectra that were present in .pdz-format, were saved as .csv-files with the “S1PXRF” software from Bruker. In order to create .txt-files readable for the fitting software, an import script from MATLAB[®] was adapted and extended to fit the needs. The script imports the csv-file and reads out the counts per channel and exports the information as a .txt-file with the same name in the same folder.

4.1 Parameters

Manufacturer:	Bruker
Model:	Tracer III-V ⁺
Detector:	Si-Pin (resolution ~190 eV at 10 000 cps)
Excitation:	Rh target x-ray tube (max. 30 μ A at 40 kV)

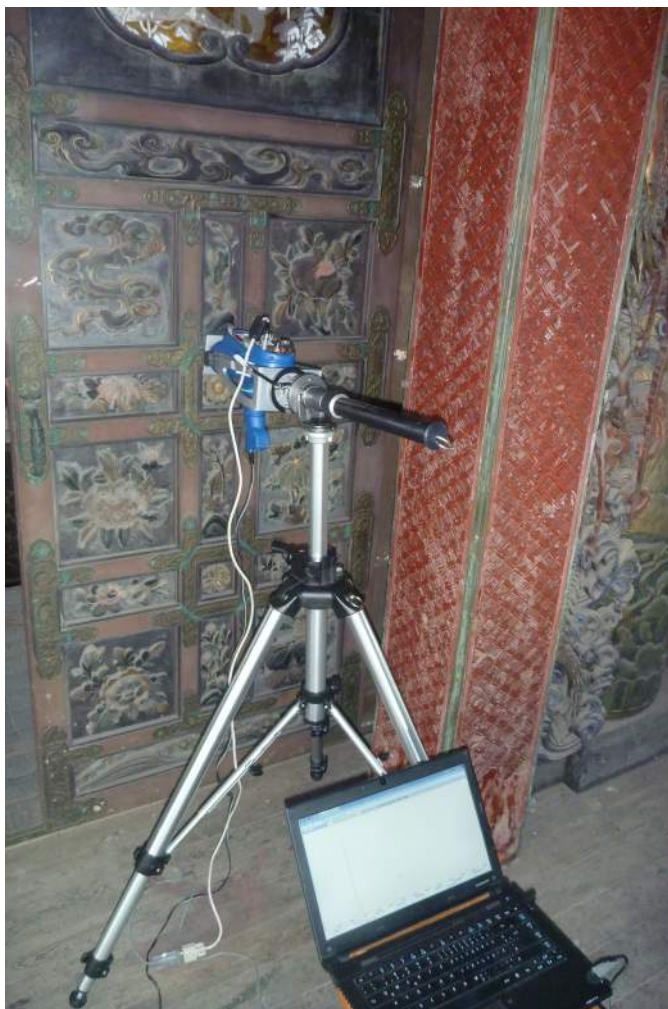


Figure 4.1: *The experimental setup in action: The Bruker Tracer III-V with the tripod and the laptop. The gilding on the door is investigated. (Experimental conditions: x-ray tube voltage: 25 kV, x-ray tube current: 2 μ A, measurement time: 250 s)*

Chapter 5

Software

Modern analytical instruments and methods require sophisticated software for efficient operation. In this chapter the different programs that were used and/or developed during this thesis are briefly discussed.

5.1 bAxil

The complex energy-dispersive x-ray spectra with frequently overlapping peaks on a large continuum need specialized spectrum analysis software. Within the research group a procedure named AXIL based on non-linear least squares fitting was developed [26]. AXIL stands for Analysis of x-ray spectra by Iterative Least squares. The AXIL concept is very well known within the XRF community and it is not by accident that the research group is called Axi²1 (Antwerp X-ray Imaging and Instrumentation Lab).

The original program was written in Fortran for a PDP-11 computer. Later developments included a version for VAX-computers. Later WinAxil was developed in C++ for running under Microsoft Windows operating systems. This version is commercialized by the company Canberra¹. The most recent version is called bAxil and is currently under development and will run on Windows, Linux and Mac platforms.

The program was used to analyze the x-ray spectra acquired during this thesis. The experience obtained was used to suggest improvements which were implemented in updated versions. Most important improvements of bAxil in comparison with WinAxil are: the possibility to fit more complex peak shapes, to fit the Compton peaks and to analyze large series of spectra obtained by line scans and image scans.

¹CANBERRA Benelux & Scandinavia (CBNS), <http://www.canberra.com/be/>

5.1.1 Evaluation of the recorded spectra with bAxil

As the spectrum data is loaded in bAxil, an .axml-file is created by the program to save the progress of the fitting process. The measurement conditions can be entered in the experimental conditions menu. Fitting model and peak shape parameters were not changed from standard values. The following figures 5.1 to 5.4 display the fitting process in individual steps.

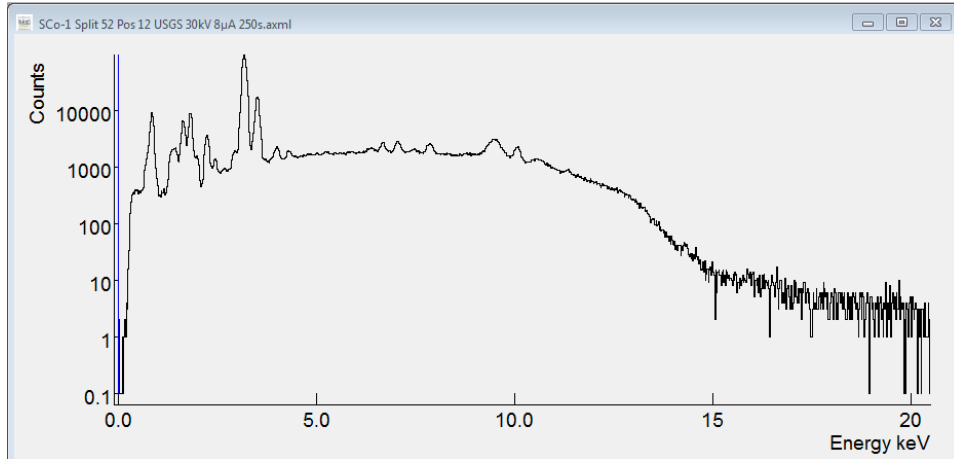


Figure 5.1: *The raw, unfitted spectra is loaded in bAxil. The y-axis is logarithmic.*

When the region of interest (ROI) is set manually, the background in the specified range is calculated (represented in green in Figure 5.2). This allows the distinction of real peaks from the background in unknown samples. When the elements of interest are known and specified priorly in the periodic table, the program calculates the net peak area and the related background automatically. The net peak area is denoted in yellow (see Figure 5.3).

The deviations of the measured to the fitted values are called residuals and can be observed in the residual plot below the spectrum. They indicate how well a spectrum is fitted. If the fit is correct the values are normally distributed with mean zero. The fitted element net peak areas can be exported into a csv-file for further data processing.

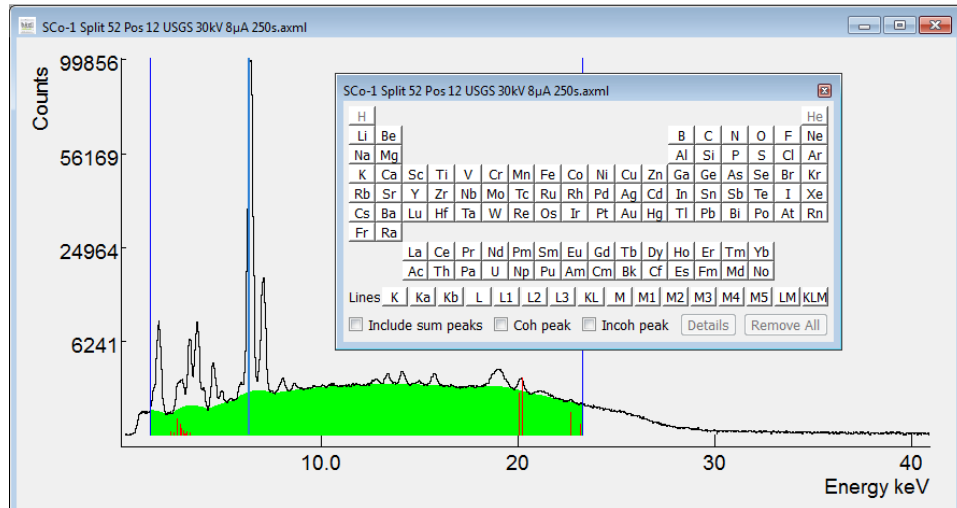


Figure 5.2: The region of interest (ROI) is set to cover the area where the elements of interest are assumed. The green area denotes the calculated background. The y-axis is now square root for better overview.

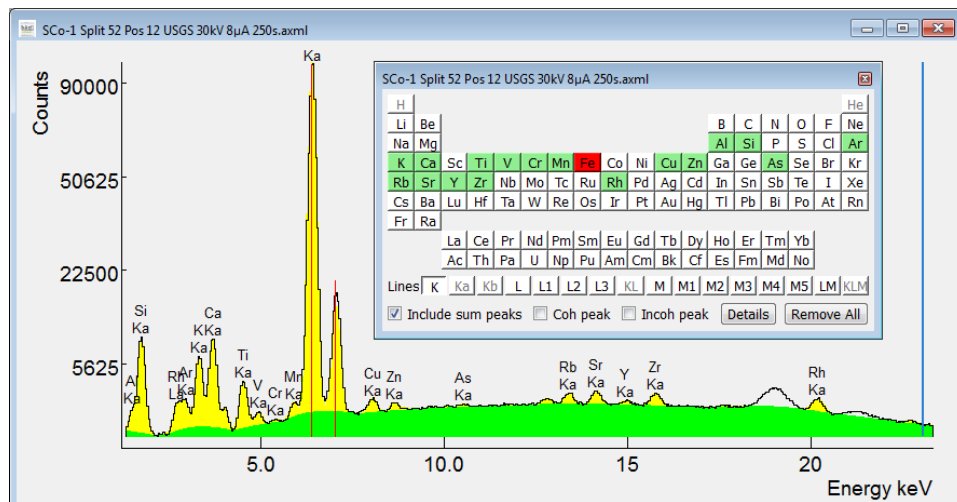


Figure 5.3: The elements can be chosen from the table of elements. When the option “Include sum peaks” is chosen, sum peaks will be fitted in the spectrum. The fit is already quite good. Only the incoherent rhodium peak (due to Compton scattering) is not fitted yet.

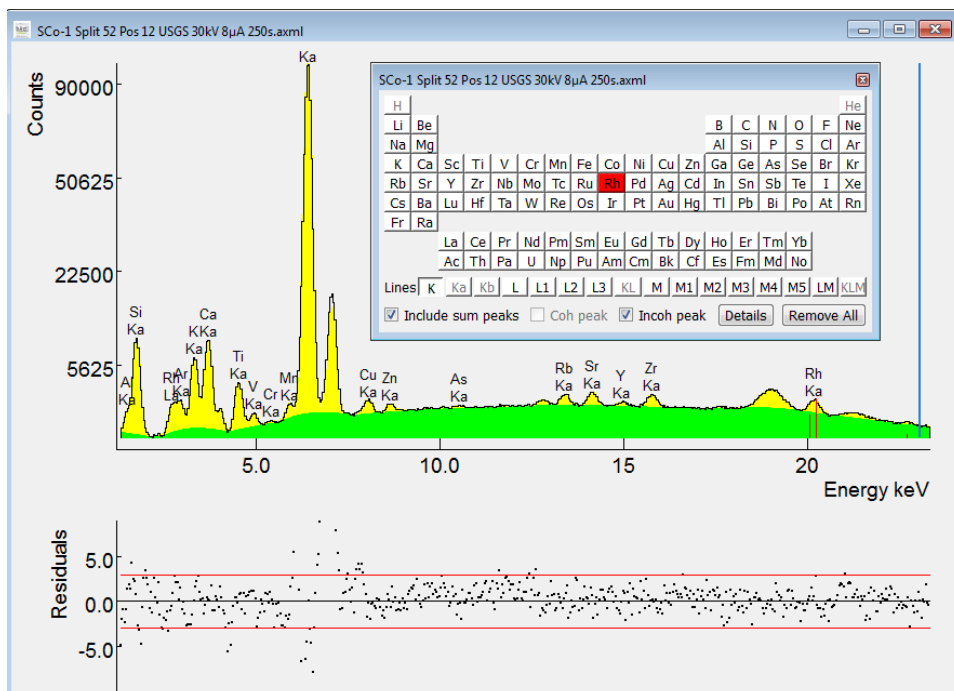


Figure 5.4: *With the fitting of the incoherent rhodium peak, the fit of the spectrum is complete. The final result is excellent, as one can see from the residual plot beneath the spectrum. The only slight deviation is found in the dominating Fe peaks and thus negligible.*

5.2 Matlab

Matlab is a so called 4 generation programming and data processing environment based on an original idea of Cleve Moler and further developed and distributed by “The MathWorks, Inc, Mass., USA”². Matlab has a very rich collection of function to do a very large variety of data analysis tasks. These are organized in toolboxes. It is also possible to develop own data processing programs by writing a so called “m-file”.

The recorded spectra from the hand-held device contained among other information the sample name, different device parameters, and the intensity per channel in a comma-separated-value-file (.csv). In order that bAxil can read and process the spectrum, a text file with the intensity per channel in a column is needed. The conversion was done with a function adapted from a script for importing data from text files. When the csv-files are given in the Matlab main directory, the function `Import_AXS_Export.m` fulfills the following tasks:

- read in the .csv-files
- extracting the intensity values
- listing the intensity values in a column according to their channel number
- writing a .txt-file with the same as the .csv-file name that contains the column

The code for the function `Import_AXS_Export.m` can be found in Appendix 11.

²<http://www.mathworks.com>

Chapter 6

United States geological survey standards

The United States geological survey (USGS) standards used for calibration purposes were available in the laboratory of the University of Antwerp. Recommended values and descriptions of the standards can be found in the certificates of analysis on the homepage of the USGS. The descriptions are cited from these certificates to give a short overview. (see reference [27–33])

Rhyolite, Glass Mountain, RGM-1

“The rhyolite, from Glass Mountain, Siskiyou County, California, was collected from a single block of massive obsidian near the terminal front of a Holocene obsidian flow. The sample is classified as a rhyolite on the basis of its high silica and total alkali contents, and it is assigned to the calc-alkali series because of its high CaO to total iron ratio.” (after *D. B. Smith* in [27])

Quartz Latite, QLO-1

“Sample for this reference material was collected in Lake County, Oregon approximately 380 km south east of Portland. The sample is derived from a lava flow on the flanks of an extrusive dome which is probably of late Miocene or early Pliocene age. The rock is greasy black and aphanitic, containing < 1% microphenocrysts of plagioclase feldspar, pyroxene, and magnetite.” (after *D. B. Smith* in [28])

Cody Shale, SCo-1

“Sample used in the preparation of this reference material was collected in Natrona County, Wyoming, near the Naval Petroleum Reserve at Teapot

Dome. SCo-1 is typical of the Upper Cretaceous silty marine shales, intermediate between fine-grained offshore shales and coarser nearshore marine siltstones. The rock is a medium dark-gray (Munsel N-4) silty shale having thin lighter colored silty laminations (Flanagan, 1976).” (after *D. B. Smith* in [31])

Mica Schist, SDC-1

“Material used in the preparation of this standard was collected in 1963 from the Washington D.C. area. The material is probably of late Precambrian age, and examination of hand specimens reveals a dark grey pervasively foliated muscovite-quartz schist with a homogeneous thinly streaked texture (Flanagan, 1976).” (after *D. B. Smith* in [32])

Dolerite, DNC-1

“Sample used in the preparation of this reference material was collected in 1968 from the Braggtown Quarry near Durham, North Carolina. The material is one of the Triassic-Jurassic olivine-normative dolerites indigenous to the area (Ragland, et al., 1968).” (after *D. B. Smith* in [30])

Diabase, W-2

“Material was collected in 1976 from the Bull Run quarry near Centreville, Virginia. This is the same collection site as USGS reference materials W-1 (Fairbairn, 1950). The diabase consists of augite and plagioclase with smaller amounts of quartz, potassium feldspar, biotite and opaque minerals.” (after *D. B. Smith* in [33])

Icelandic Basalt, BIR-1

“Material for this reference material was collected from one of the interglacial lava flows often referred to as the Reykjavik dolerites, by Karl Gronwold of the Nordic Volcanological Institute at Reykjavik (Flanagan, 1984). The Reykjavik dolerites are a group of lava flows most likely from shield volcanos dating from the youngest interglacial periods. The rock is as a coarse-grained olivine tholeiite.” (after *D. B. Smith* in [29])

Part III
Methods

Chapter 7

Quantitative analysis of samples by XRF

For the understanding of the analytical aspects of x-ray fluorescence, a basic knowledge of the fundamental relations is necessary. A brief introduction is given on the following pages.

In 1955 the mathematician Jacob Sherman developed an equation, which is able to calculate the net XRF intensities of each element from a sample with known composition, when it is irradiated by a polychromatic x-ray beam. [34] The equation has the form of

$$I_i = f (c_i, c_j, c_k, \dots, c_n)$$

where I_i and c_i are the intensity respectively the concentration of element i . However, the objective of the XRF quantification techniques is reciprocal, thus the conversion of XRF intensities to the specimen composition in terms of analyte concentrations. Unfortunately, the reversion of the equation ($c_i = f (I_i, I_j, I_k, \dots, I_n)$) is not valid. Actually the relation is more complicated, since a variety of aspects has to be considered. The net intensities also depend on the sample (solid, liquid or powder), accompanying elements (matrix effect!), preparation, surface texture, homogeneity as well as instrumentation related issues like measurement conditions, detector efficiency, flux and spectral distribution of the x-ray tube.

7.1 The fundamental parameter relation

Mathematical methods like the fundamental parameter method use the insights of the Sherman equation to calculate the matrix effect rather than measuring it. Hereinafter the basic relations between the incoming radiation and the detected signal of the sample are described. The measured intensity (in cps) of any given K_α (we assume Fe in an Al matrix here) radiation can be summed up in three factors:

I. Amount of primary x-rays that reach a certain depth

The primary x-rays of Energy E_0 that are remaining in the sample at a layer dx at depth x are given by

$$I_x = I_0 \cdot e^{-\frac{\mu(E_0) \cdot \rho \cdot x}{\sin \theta_{in}}} \quad (7.1)$$

where I_x denotes radiation intensity at layer dx at a depth x perpendicular to the sample surface, I_0 the incident Intensity, μ the mass absorption coefficient of the sample-matrix, ρ the density and θ_{in} the incident angle. The term

$$\frac{x}{\sin \theta_{in}} = l_{in}$$

in Equation 7.1 describes the actual traveled path (l) in the sample. We are assuming a homogeneous specimen and (monochromatic) parallel focused incident radiation. The calculation of the mass absorption coefficient μ for an Fe-Al matrix (see Figure 7.1) is according to Equation 2.4 on page 27:

$$\sum_{i=1}^n \mu_i(E_0) \cdot w_i = \mu_{Fe}(E_0) \cdot w_{Fe} + \mu_{Al}(E_0) \cdot w_{Al} \quad (7.2)$$

where μ_i is the mass attenuation coefficient and w_i the weight fraction for an element i .

II. Number of K -vacancies created and resulting amount of emitted K_α -photons

For the analyte of interest, Fe, the amount of vacancies created in the sample is

$$dI_{Fe} = f_{K_\alpha} \cdot \omega_K \left(1 - \frac{1}{J_K}\right) \tau_{Fe}(E_0) \cdot \rho_{Fe} \cdot \frac{dx}{\sin \theta_{in}} \cdot I_x \quad (7.3)$$

where the term

$$\tau_{Fe}(E_0) \cdot \rho_{Fe} \cdot \frac{dx}{\sin \theta_{in}} \cdot I_x$$

refers to the amount of Fe vacancies created in the layer dx in depth x , with ρ_{Fe} the “density” of iron in grams Fe per cm^3 and τ_{Fe} denotes the number of vacancies created through photo electric absorption in the Fe Atoms in the sample. The term

$$\left(1 - \frac{1}{J_K}\right) \cdot \tau_{Fe}$$

describes the fraction of K -shell vacancies with J_K the K -shell jump ratio of Fe. J_K can be calculated through

$$J_K = \frac{\tau_+(\Phi_K)}{\tau_-(\Phi_K)}$$

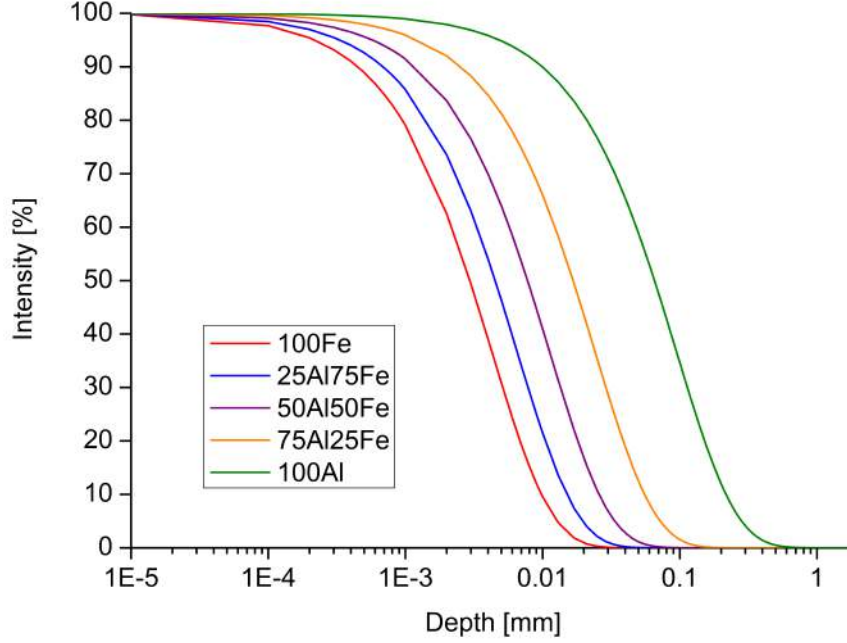


Figure 7.1: Attenuation for primary x-rays in different Fe-Al matrices

where τ_+ resp. τ_- is the cross section before and after the K absorption edge. ω_K is the K -shell fluorescence yield of Fe and f_{K_α} the fraction of K_α photons emitted in relation to all the photons from the K -shell (thus $K_\alpha + K_\beta$ combined).

III. Amount of K_α -photons able to leave the specimen and reach the detector

The number of Fe K_α photons which are detected depends on the length of the path they travel in the specimen, the air path and the detector efficiency. Expressed as an equation this becomes

$$dI_{FeK_\alpha} = \frac{\Omega}{4\pi} \cdot \epsilon(FeK_\alpha) \cdot e^{-\frac{\mu(FeK_\alpha) \cdot \rho \cdot x}{\sin \theta_{out}}} \cdot dI_{Fe} \quad (7.4)$$

where

$$\frac{x}{\sin \theta_{out}} = l_{out}$$

denotes the path of the Fe K_α photons in the specimen, the exponent

$$-\frac{\mu(FeK_\alpha) \cdot \rho \cdot x}{\sin \theta_{out}}$$

describes the attenuation of the Fe K_α x-rays from a depth x , $\frac{\Omega}{4\pi}$ the fraction of characteristic x-rays seen by the detector and $\epsilon(FeK_\alpha)$ stands for the attenuation due to the air path and the Be window of the detector.

If the three Equations 7.1, 7.3 and 7.4 are combined and integrated over the sample thickness d , the intensity of Fe K_α from the entire specimen becomes:

$$I_{FeK_\alpha} = G \cdot S_{Fe} \cdot \rho_{Fe} \cdot I_0 \cdot \left[\frac{1 - e^{-\chi \cdot \rho \cdot d}}{\chi \cdot \rho} \right] \quad (7.5)$$

The following constants have been grouped:

$$\frac{\Omega}{4\pi \sin \theta_{in}} = G \quad (7.6)$$

is the geometric factor G ,

$$\frac{\mu(E_{FeK_\alpha})}{\sin \theta_{out}} + \frac{\mu(E_0)}{\sin \theta_{in}} = \chi \quad (7.7)$$

is the absorption term for the in- and outgoing radiation.

$$\epsilon(FeK_\alpha) \cdot K_{Fe} \cdot \tau_{Fe}(E_0) = S_{Fe} \quad (7.8)$$

can be considered the sensitivity of element Fe. Therein

$$f_{K_\alpha} \cdot \omega_K \left(1 - \frac{1}{J_K} \right) = K_{Fe} \quad (7.9)$$

describes the fundamental constants as K_{Fe} . Finally, if we consider an infinite thick sample, $d \rightarrow \infty$ therefore the exponent of Equation 7.5 becomes zero and after rewriting

$$\frac{\rho_{Fe}}{\rho} = w_{Fe}$$

where w_{Fe} is the weight fraction of Iron, the final equation reveals the measured intensity for the K_α radiation in an “infinite” thick sample:

$$I_{FeK_\alpha} = G \cdot S_{Fe} \cdot I_0 \cdot w_{Fe} \cdot \frac{1}{\chi} \quad (7.10)$$

In the above derivations, the following assumptions have been made (after *de Vries and Vrebos* in [9]):

1. The specimen is completely homogeneous.
2. The specimen extends to infinity in three dimensions.
3. The primary rays are not scattered on their way to the layer dx .
4. No enhancement effects occur.
5. The characteristic radiation is not scattered on its way to the specimen surface.

Chapter 8

Calibration and correction procedures

Correction methods are applied to the raw data to reduce influences that alter the analyte signal. In situations where quantitative XRF results are desired, calibration procedures are used. This chapter explains the methods and procedures used in this work.

8.1 Estimation of the regression parameters

When preparing standards for calibration, the error during preparation is most often negligible in contrast to the measurement error. Therefore calibrations are regarded as Model I regressions with no error in the independent variable x . If the true relation is assumed to be a straight line, the model to describe it is:

$$\eta = \beta_0 + \beta_1 \cdot x \quad (8.1)$$

where η is the response, β_0 and β_1 respectively the parameters for the *intercept* and *slope* of the true (but unknown) regression line. The true response might be known, but the fact, that every measurement is subject to errors, forces us to add an additional factor ε_i , which represents the error of the dependent measurement variable y_i :

$$y_i = \beta_0 + \beta_1 \cdot x + \varepsilon_i \quad (8.2)$$

Since β_0 and β_1 are unknown, we can only estimate them by using the information gained by the measurements. The parameter b_1 and b_0 are calculated in a way that the estimated regression line is designed to fit the experimental data points as well as possible:

$$\hat{y} = b_0 + b_1 \cdot x \quad (8.3)$$

It is obtained by minimizing the sum of squares of the residuals with the *least-square method*. For this equation exists only *one* smallest solution:

$$R = \sum e_i^2 = \sum (y_i - \hat{y}_i)^2 \quad (8.4)$$

where R is the sum of the squared residuals, and \sum is the reduced expression for $\sum_{i=1}^n$ with n the number of observed data pairs. The *residuals* e_i represent the deviation between the response of the measurement y_i and the prediction from the regression line \hat{y}_i . Each data point has one residual:

$$e_i = y_i - \hat{y}_i \quad (8.5)$$

If Equation 8.4 is differentiated with respect to b_1 and b_0 and set to zero, the expressions for b_1 and b_0 can be obtained:

$$b_1 = \frac{\sum (x_i - \bar{x}) \cdot (y_i - \bar{y})}{\sum (x_i - \bar{x})^2} \quad (8.6)$$

$$b_0 = \bar{y} - b_1 \cdot \bar{x} \quad (8.7)$$

where $\bar{y} = (\sum y_i)/n$ the mean of all y_i and \bar{x} the mean of all x_i respectively.

The *residual variance* s_e^2 is the variance in the signal which cannot be accounted for by the regression line. It is an indicator of the spread of the response when x has already been taken into account.

$$s_e^2 = \frac{\sum (y_i - \hat{y}_i)^2}{n - 2} \quad (8.8)$$

If the least square method is applied, it is assumed that the dependent variables have the same variances σ^2 . In other words, the precision of the measurement is independent of the concentration. This uniform variance is called *homoscedasticity*. There are two other conditions that have to be met [35]:

- for each x_i the residuals e_i are from a population that is *normally distributed* with mean zero.
- the e_i are independent.

8.2 General calibration equation in XRF analysis

The most straight forward way to relate the measured intensity I_i with the concentration w_i is through a linear model:

$$I_i = b_0 + b_1 \cdot w_i \quad (8.9)$$

b_0 and b_1 are model parameters which are estimates for the intercept and the slope of the true regression line (which is unknown). As seen in the

previous section, the relationship between intensity and concentration is quite complicated and is in the least often cases a straight line (see Figure 8.1 on page 56). Linear approximations therefore are only useful in a very small range of concentrations for very similar samples. A better, more widely applicable approach is thus favored.

For XRF analysis the general calibration equation has to address the different relationships adequately (after *de Vries and Vrebos* in [9] and *Weltje et al.* in [7]):

$$W_{ij} = K_j \cdot I_{ij} \cdot M_{ij} \cdot S_i \quad (8.10)$$

The above equation yields the analyte concentration of the element j in a sample i , if the device-specific constant K_j , the measured element intensity I_{ij} , the matrix effect M_{ij} and the specimen effect S_i are known. A closer look at the parameters reveals their influence:

The device specific constant K_j is a calibration constant, that defines the sensitivity (i.e. excitation and detection efficiency) for an element j .

The measured element intensity I_{ij} refers to the deconvoluted, integrated peak, which is already sum- and escape-peak corrected. This is done by a spectrum analyzing software e.g. bAxil.

The specimen effect S_i captures the measurement geometry and thus the homogeneity in terms of element distribution and surface smoothness. Two mutually influencing issues have to be kept in mind: the larger the scanned surface area is, the higher is the probability, that it is not smooth anymore. Conversely, if the spatial resolution is very high, the irradiated area is smaller and thus might not display the over all composition properly. In practice, the chosen settings are somewhere in between, but for meaningful results, the resolution should be well above the size of the largest sediments.

Under well constraint laboratory conditions the specimen effect S_j is almost constant, since the sample is usually dried, powdered, homogenized and pressed to a pellet. A destructive analysis however, is often not wanted respectively due to time and space issues, not always possible. K_i is a constant and W_{ij} is calculated from post-processed intensity I_{ij} . The matrix effect M_{ij} in the above equation can be seen as a correction factor.

The matrix effect M_{ij} covers the enhancement and absorption effects of the primary and/or the characteristic x-rays due to variations in chemical composition (see Figure 8.1).

The *absorption effect* is best explained in the theoretical case of only two compounds (analyte and matrix). It can be separated in three cases (compare with table 8.1):

1. If the absorption coefficient is (nearly) equal for the matrix and analyte, a linear dependence between intensity I and analyte concentration w_j is obtained.
2. In cases where the matrix element has a higher absorption coefficient for both, the characteristic radiation of the analyte and the primary x-rays, the analyte signal is lower due to absorption. This is known as *positive* absorption.
3. On the contrary, if the matrix elements absorb less than the analyte, the intensity of the analyte signal is higher. This is called *negative* absorption.

Table 8.1: *The Classification of the three different absorption effects*

Matrix absorbs:		Analyte absorbs:	Absorption
primary + analyte	>	primary + matrix	positiv
primary + analyte	<	primary + matrix	negativ
primary + analyte	=	primary + matrix	linear

The *enhancement effect* describes the phenomenon, that the characteristic x-ray intensity of an analyte element is enhanced through secondary excitation from the radiation of matrix elements. The enhancement effect is usually smaller than that of positive or negative absorption [9]. This occurs if the K_α fluorescence energy of a matrix element is slightly higher than the absorption edge of the observed element. In a sample that contains e.g. Ni, Fe and Cr, the Ni K_α rays are just above the K absorption edge of Fe. In this energy region, Fe shows a high mass absorption coefficient, thus absorbing the Ni K_α radiation and enhancing the Fe signal. The same with the Fe K_α rays and the K absorption edge of Cr.

As indicated earlier, K_j and S_i are constant under laboratory conditions, thus leaving the majority of the interference to the matrix effect. It would be desirable if a way can be found to either evaluate or eliminate this effect.

8.3 Straight line regression analysis and calibration

Straight line *regression analysis* is used to investigate the relationship between two or more variables. The mathematical function which is used for this purpose can also be taken to predict one variable from the other(s). There are two possible models:

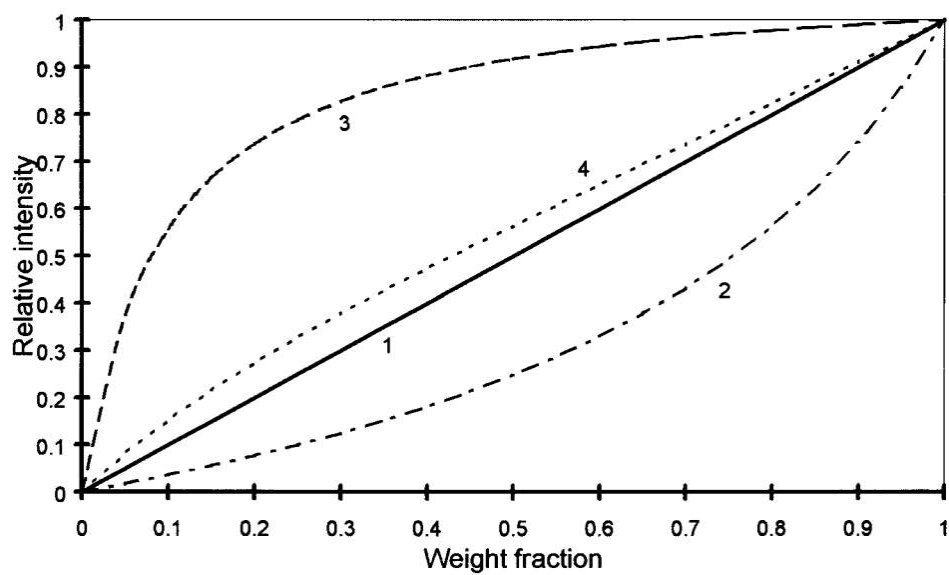


Figure 8.1: *Different matrix effects that can be observed in calibration curves: 1: no net-matrix effect, 2: positive absorption (net absorption of the analytes radiation by the matrix), 3: negative absorption (net absorption of the analytes radiation by the analyte), 4: enhancement effect (enhancement of the analytes radiation by the matrix, see section 8.2 on page 53) (after R. Van Grieken in [9])*

Model I regressions are used to study the relation between a random variable (called *dependent* or *response variable*) and a variable controlled by the researcher (called *independent* or *prediction variable*), which is assumed to be without error. It is either exactly known or preselected. The most important application of this model is the *calibration*, which tries to predict the concentration of an unknown sample, based on the instrumental response that is related to the known analyte concentration in calibration standards.

Model II regressions are used in case where both variables are subject to error, e.g. in comparison studies (after *D. L. Massart* in [35]).

In general, a good knowledge about the relation of the two variables is needed in order to give the regression parameters a physical meaning. In cases where no information is available, empirical parameters can be used. The true scientific meaning might be unknown then, but nevertheless they can be very useful for prediction and are most often used [35].

8.4 The Compton corrected matrix effect

In 1958 G. Andermann and J. W. Kemp proposed a new calibration method to reduce both, the influence of the absorption effect and the device specific constant. Observations indicated, that the amount of scattering I_s is inversely proportional to the mass-attenuation coefficient of the matrix μ_s :

$$I_s(\lambda_s) \propto \frac{1}{\mu_s(\lambda_s)} \quad (8.11)$$

They normalized the spectra of different Ni-ores by dividing them through the intensity of the incoherent scatter peak (Compton peak). They were able to obtain a linear relationship between the intensity and the concentration of Ni in the ores (Figure 8.2), even though the Fe-content of the matrices varied between 10 and 65%.

The mathematical relationship is expressed as following:

$$\frac{I_i}{I_{Inc}} = b_0 + b_1 \cdot w_i \quad (8.12)$$

This normalization remedies variations in the surface, grain size effects as well as current and tube voltage differences, if the variation of the matrix effect is largely attributed to absorption effects. It can not however, correct for enhancement effects in the sample. Since the Compton peak is much more intense for light elements, this method is mainly used in determination of geological samples that consist of oxides.

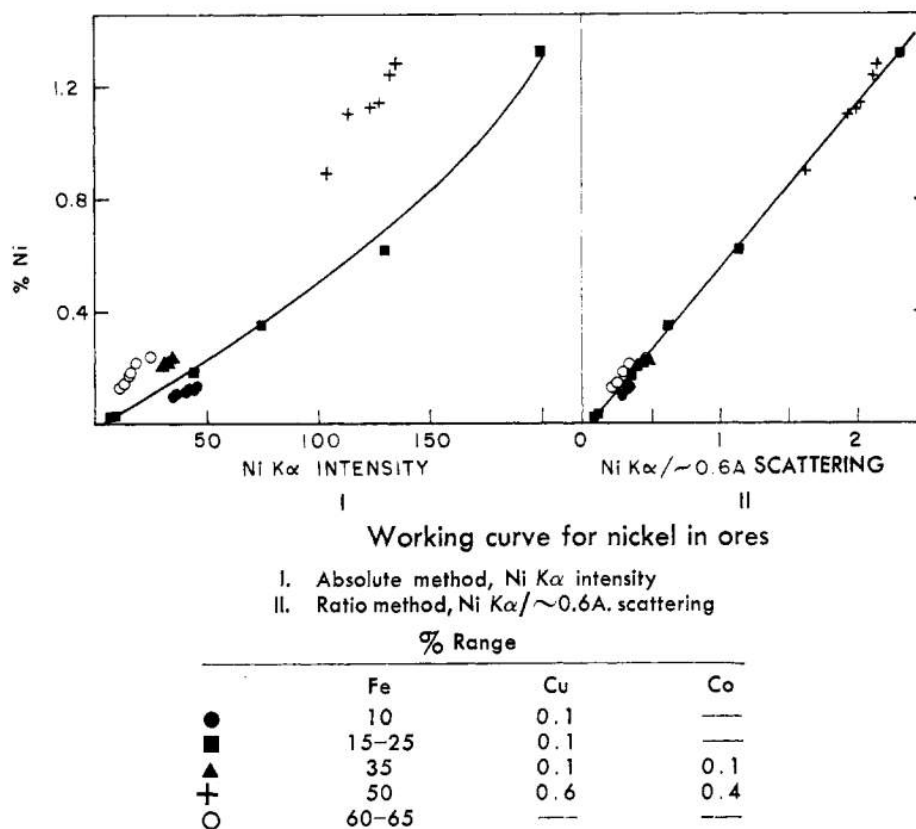


Figure 8.2: Use of the Compton peak as internal calibration (see description above) for Ni ores with different Fe containing matrices. Left: weight fraction Ni vs. net-intensity Ni K α , right: weight fraction Ni vs. ratio Ni K α intensity / 0.6 A scatter peak. The improvement of the calibration line is clearly visible (after G. Andermann and J. W. Kemp in [36])

8.5 Compositional data

The theory of compositional data is based on a few basic concepts.

A comparison between two samples without normalization cannot be used to make a point about the composition. For a reasonable comparison, the data has to be closed, meaning the components have to be summed up to a constant κ which is either 1 or 100 (percent). In other words, the sum of all elements in the sample has to sum up to unity. This closure constraint specifies:

$$\sum_{i=1}^D x_i = 1 \quad \text{with } x_i > 0 \quad (8.13)$$

where D is the actual number of elements in the sample and x_i is the weight fraction of element i .

In practice however this is not the case, since only a limited range of elements can be detected by XRF devices, regardless of their construction. Therefore we are dealing with subcompositions instead of “the whole”. Considering this circumstance, Equation 8.13 reads as follows:

$$\sum_{i=1}^m x_i + \sum_{j=m+1}^D x_j = \kappa \quad \text{with } x_i > 0 \quad (8.14)$$

where D represents the total number of elements present in the sample, and m the elements detectable ($m < D$).

To elucidate the problem of sub-compositions within compositional data, a trivial case of three-part composition is given (after *R. Tjallingii, et. al.* in [37]): The upper part of figure 8.3 on page 60 shows the intensity of three elements A, B and C (indicated as red, green and blue) present in different sample positions. While elements B and C are unchanged, A varies. If this relation is now expressed in concentration, *all* element concentrations change relative to the whole (bottom part). In the case that one of them is not detected, the concentrations are erroneous.

In summary, with the poorly constrained measurement geometry S_i and the elements not detectable, the use of Equation 8.10 (page 54) is problematic.

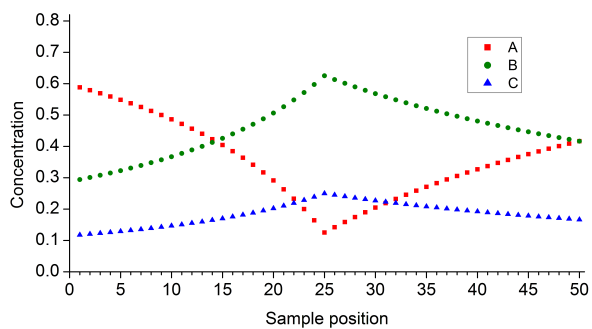
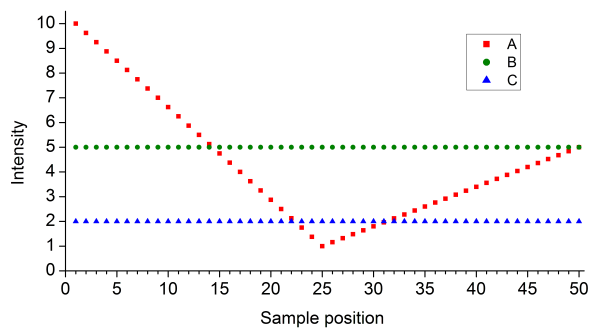


Figure 8.3: *The upper part shows the intensity of three elements A, B and C present in different positions of the sample. While elements B and C are unchanged, A varies. If this relation is expressed in concentrations, all element concentrations change relative to the whole.*

8.6 Elemental ratios

An interesting alternative offers the use of element-intensities-ratios for calibration rather than plain single-element intensities. A comparison in terms of ratios offers the benefit of having a form of closure that is unbiased and unaffected by the other elements in the sample. Figure 8.4 shows the ratios of the three elements(A/B, A/C and C/B). It reflects the relationship between each element correct. If in this depiction an element is not detected, the ratio A/B of the elements is still true, since ratios are independent from each other.

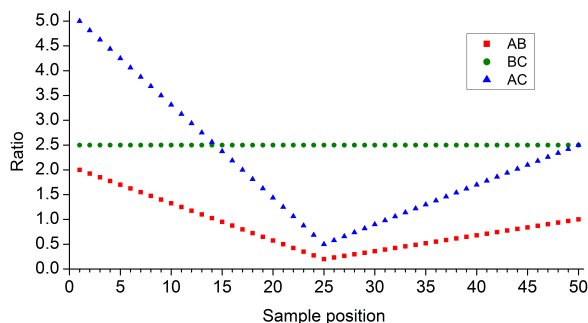


Figure 8.4: The ratios of three elements A/B , C/B and A/C (denoted as AB , CB and AC) are shown. The relationship between each element is correct, even if e.g. C is not detected, the elemental ratio A/B is still true.

Another good example where element ratios are beneficial are in case of surface water films, which form under protective foils of drill cores of marine sediments. It is known that they influences the intensities of lighter elements such as Al and Si which are major components of such samples [38]. When expressed as ratios however, this noise factor disappears, along with other specimen related interferences of S_i . With the elemental ratios (e.g. Al/Si) applied on the standard calibration equation, it becomes clearly visible why:

$$\begin{aligned} \frac{W_{Al,i}}{W_{Si,i}} &= \frac{K_{Al}}{K_{Si}} \cdot \frac{I_{Al,i}}{I_{Si,i}} \cdot \frac{M_{Al,i}}{M_{Si,i}} \cdot \frac{S_i}{S_i} \\ \frac{W_{Al,i}}{W_{Si,i}} &= \frac{K_{Al}}{K_{Si}} \cdot \frac{I_{Al,i}}{I_{Si,i}} \cdot \frac{M_{Al,i}}{M_{Si,i}} \cdot 1 \end{aligned} \quad (8.15)$$

The specimen effect S_i is for every element at a position i the same and thus the *relative* specimen effect becomes one. More often than one thinks the knowledge of the actual concentration is irrelevant, since the focus lies on the *change* of composition (or properties) not the composition itself. Although elemental ratios are an important contribution towards solving the closed

sum issue, their asymmetry ($A/B \neq B/A$) gives rise to the question, which element the numerator respectively the denominator should be. This issue was solved by Aitchison [39, 40], by performing a *logarithmic transformation* on the elemental ratios. Logarithmic ratios are symmetrical ($A/B = B/A$, see Figure 8.5), thus a statement derived by analysis of A/B is also valid for B/A . The results of statistic analysis are hence free of arbitrary decisions.

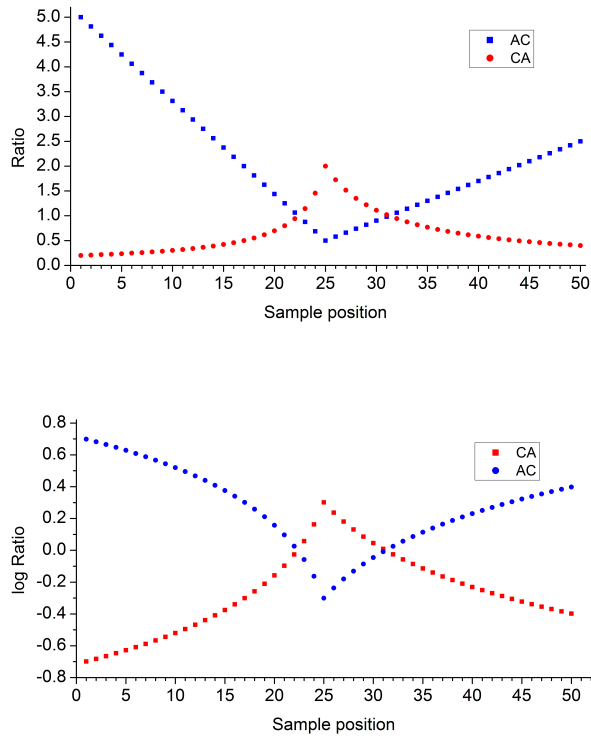


Figure 8.5: While ratios ($A/C = AC$, $C/A = CA$) have the undesirable property of being asymmetrical, log-ratios are fully symmetrical.

8.7 The log-ratio calibration equation

This section illustrates the development of the log-ratio calibration equation as proposed in the paper of *Weltje et al.* ([7], chapter 6).

The first step towards the LRCE was already stated in Equation 8.15 on page 61. Two general calibration equations have been combined, resulting in the eradication of the critical factor of the standard calibration, the specimen effect s_i . Elements indicated by subscripts j and D , the measurement resp. the specimen is denoted with subscript i . The relative detection efficiency and the relative matrix effect is introduced:

$$\tilde{K}_{jD} = \left(\frac{K_j}{K_D} \right), \tilde{M}_{ijD} = \left(\frac{M_{ij}}{M_{iD}} \right) \quad (8.16)$$

resulting in:

$$\frac{W_{ij}}{W_{iD}} = \tilde{K}_{jD} \cdot \left(\frac{I_{ij}}{I_{iD}} \right) \cdot \tilde{M}_{ijD} \quad (8.17)$$

The relative detection efficiency \tilde{K} does not change with i , it is considered an average response during scanning and depended on elements j and D . The relative matrix effect \tilde{M} changes with i , the element composition. M is unknown, but most likely strongly non-linear. Often no information is available a priori, thus \tilde{M} should stand for the non-linear relation of intensities and concentrations:

$$\tilde{M}_{ijD} = \left(\frac{I_{ij}}{I_{iD}} \right)^{A_{jD}} \quad (8.18)$$

Condensing Equation 8.18 into Equation 8.17 yields:

$$\frac{W_{ij}}{W_{iD}} = \tilde{K}_{jD} \cdot \left(\frac{I_{ij}}{I_{iD}} \right)^{A_{jD}+1} \quad (8.19)$$

Equation 8.19 is a shortened form of Equation 8.15 (page 61) where ratios of (relative) net intensities are expressed as a non-linear function of ratios of concentrations. A logarithmic transformation of Equation 8.19 is necessary to gain the compositional data space:

$$\ln \left(\frac{W_{ij}}{W_{iD}} \right) = \alpha_{jD} \cdot \ln \left(\frac{I_{ij}}{I_{iD}} \right) + \beta_{jD} \quad (8.20)$$

where

$$\alpha_{jD} = A_{jD} + 1$$

and

$$\beta_{jD} = \ln \left(\tilde{K}_{jD} \right)$$

Equation 8.20 is finally the *log-ratio calibration equation (LRCE)* which is a fully non-dimensional standard linear equation. α is thus the analogous of the slope, while β is the analogous of the intercept in a standard

linear equation. It is free of unit-sum and non-negativity constraints, since intensity I and weight-percent W are only considered in dimensionless log-ratios [7]. As mentioned before in section 8.1 (on page 52), the error during preparation of standards is most often negligible in contrast to the measurement error. The error is ascribed solely to the dependent variable y , which is the measured intensity in our case. Thus variables I and W have to be interchanged. This results in:

$$\ln \left(\frac{I_{ij}}{I_{iD}} \right) = \alpha_{jD} \cdot \ln \left(\frac{W_{ij}}{W_{iD}} \right) + \beta_{jD} \quad (8.21)$$

With Equation 8.21 the correct model I regression can be calculated when W is known and I is measured.

Part IV

Results and discussion

Chapter 9

Micro XRF setup

The measurements with the micro XRF setup pursued the ultimate goal to determine whether the LRCE method is preferable when calibrating samples. See the results in section 9.3. Since the setup was rebuilt due to a relocation, it had to be reconfigured. Section 9.1 addresses the long term stability of the setup in terms of count detection. The line scans approached in section 9.2 review if the manufactured standards are homogeneous. Section 9.4 applies the classic and the LRCE calibration method on a unspecified rock sample that was available in the laboratory.

For a brief description of the USGS standards see chapter 6 on page 45.

9.1 Drift measurements

To test the laboratory micro XRF setup for drift phenomena over a longer time period, the USGS¹ standards were measured consecutively 500 times in one spot (the center). In figure 9.1 the total countrate of the fitted RGM-1 Spectrum can be observed. The over all count rate decreases slightly with the number of measurements. Each dot represents a single measurement. The vertical error bars indicate the standard deviation of the uncertainty during the fitting process. Note the discontinuation of the y-axis.

Figure 9.2 shows in detail the intensity progression of the ten element sub-composition of the RGM-1 standard. Note that the y-axis is logarithmic, thus the elements with lower countrate (hence counts) appear to have greater noise. Since a drift is not visible to the naked eye, the slope of each element intensity has been calculated separately to gain a more objective way to look on the data.

Table 9.1 presents the slopes of the raw intensities of the 10 element sub-composition of the USGS standards. The calculated slope values show

¹abbr.: United States Geological Survey

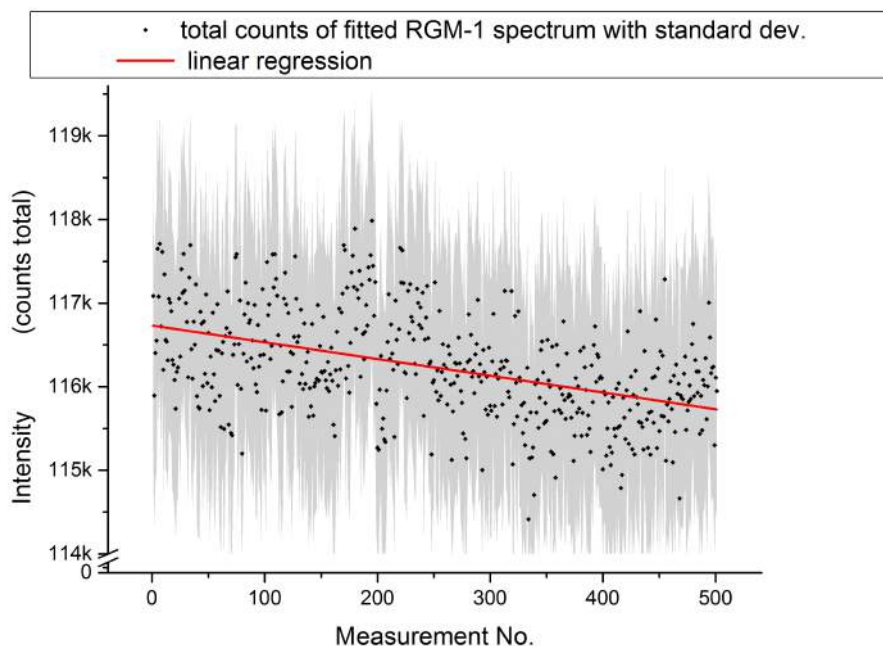


Figure 9.1: Total countrate of the fitted RGM-1 Spectrum. Its trend is dominated by the strongest signal , the FeK_{α} peak, which's intensity is decreasing in the beginning. Each dot represents a single measurement, the semitransparent area refers to the standard deviation.

almost no change in intensity over the span of 500 measurements, except for the FeK_{α} peaks.

As shown in Figure 9.3, the drift of the FeK_{α} signal in the beginning is quite high. After the first 20-40 measurements, the intensity remains constant. This problem can be eradicated by correcting the raw intensities with the Compton scatter peak. The corrected slope values are given in Table 9.2. Compared to the raw data, the change in intensity is almost zero after correction.

Figure 9.2 on page 68 shows as an example the element drifts of the 10 element sub-composition of standard RGM-1. The scale is logarithmic to fit all 10 elements in the figure. Since the distinction of an eventual slight change in the intensity during the drift measurements is subject to the viewers eye, the calculation of the slope is more objective. The values for all seven standards are given in Table 9.1.

A look an Table 9.1 on page 68 reveals that the slope and hence the overall change of the signal is low. An exemption is the Fe signal, that has a considerable change. Figure 9.3 reveals the drift in the beginning. In general elements with a strong signal/noise ratio show more drift respectably change in signal than low count rate elements.

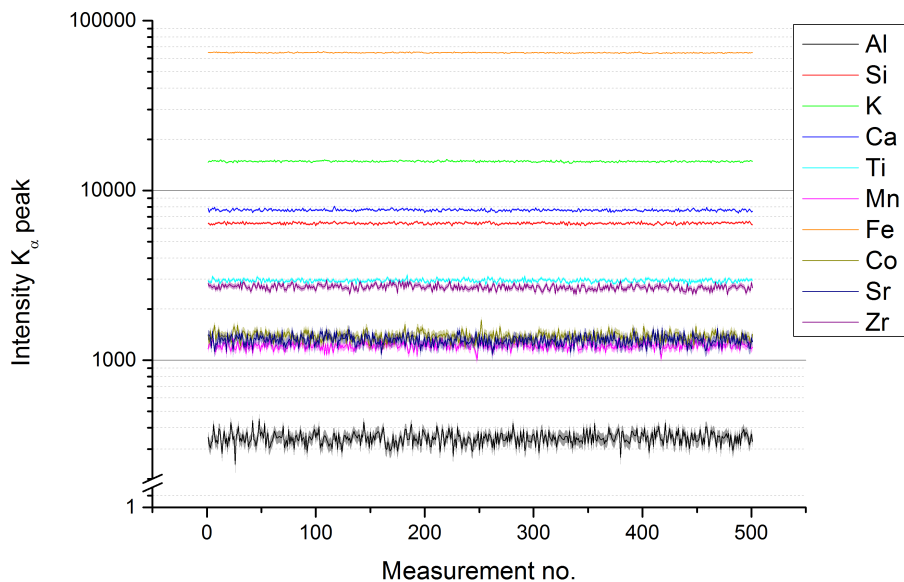


Figure 9.2: Intensity of the 10 element sub-composition in the RGM-1 standard. A change in intensity during the measurements is not visible. Note the logarithmic y-axis. The standard deviations of the measurements are semi-transparent

Table 9.1: Slope of the raw intensities of the 10 element sub-composition of the USGS standards (see chapter 6). The calculated slope values show very little change in intensity, except for the iron signals

	RGM-1	QLO-1	SCo-1	SCD-1	DNC-1	W-2	BIR-1
Al K_α	0.009	-0.025	0.018	0.001	-0.008	0.007	0.001
Si K_α	0.005	-0.030	0.077	0.118	-0.055	0.029	-0.022
K K_α	-0.172	-0.316	0.160	0.042	-0.018	-0.081	0.004
Ca K_α	-0.098	0.379	0.158	-0.004	-0.785	-1.323	-0.566
Ti K_α	-0.024	0.131	0.099	-0.050	-0.099	-0.205	-0.070
Mn K_α	0.013	0.106	0.073	-0.003	-0.018	-0.184	-0.036
Fe K_α	-0.727	1.342	2.466	0.235	-4.008	-7.161	-1.399
Co K_α	-0.039				-0.011		
Sr K_α	-0.048	0.367	0.014	-0.041	-0.063	-0.080	-0.024
Zr K_α	-0.148	-0.005	0.046	0.007	0.028	-0.078	0.023

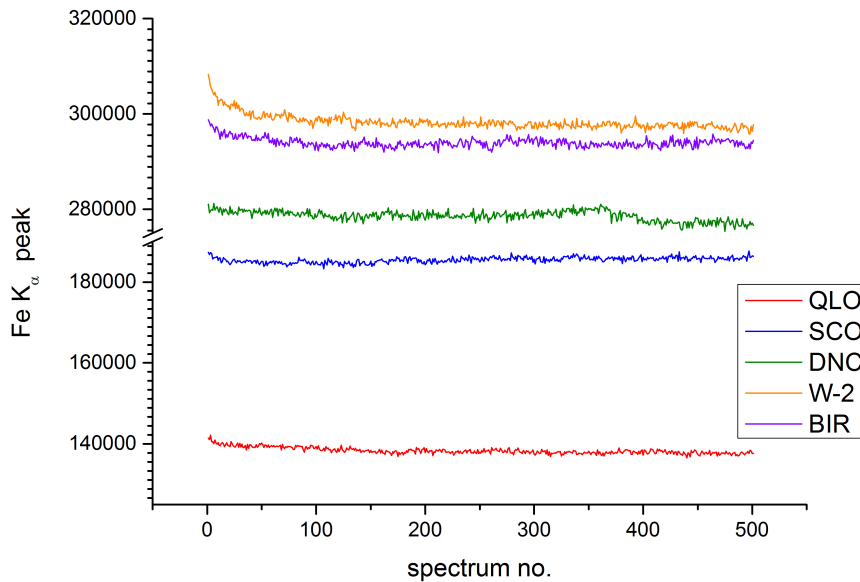


Figure 9.3: *Drift of the intensity of the $Fe K_{\alpha}$ peaks during the 500 consecutive measurements. Especially for high count rates (higher Fe content) the drift in the beginning is considerably larger. The slope stems most probably from the x-ray tube, when a “cold” start is performed.*

Figure 9.3 shows that for the first 20 to 50 measurements the Fe count rate is slightly higher, especially for high count rates like for standards W-2 and BIR-1. For standard DNC-1 an edge is noticeable around spectrum number 350. This reflects upon the slope value of standard DNC-1. Since no parameters weren’t changed during measurement, the slope stems most probably from the x-ray tube, when a “cold” start is performed.

When correcting the raw intensity values with the incoherent Compton peak, the drop in the beginning is eradicated. The corrected values are depicted in Table 9.2 on page 70.

9.2 Line scans

The line scans of the USGS standards were carried out to check the homogeneity of the prepared standards. To accomplish the task, the sample stage was programed to take a step after every measurement. In total 101 measurements were carried out, whilst moving in a straight line over the surface of the standard. Table 9.3 displays the mean and the standard devi-

Table 9.2: Slope of the Compton corrected intensities of the 10 element sub-composition within the 500 measurements of the USGS standards (see chapter 6). With the corrected intensity values, the change in intensity is close to zero and thus negligible.

	RGM-1	QLO-1	SCo-1	SCD-1	DNC-1	W-2	BIR-1
Al K_α	7.15E-06	3.03E-07	-9.94E-07	1.72E-06	6.72E-06	1.57E-05	5.44E-06
Si K_α	1.07E-04	3.38E-05	-5.31E-05	5.08E-05	5.48E-05	1.54E-04	3.49E-05
K K_α	2.12E-04	8.79E-05	-1.12E-04	5.65E-05	2.24E-05	7.85E-05	8.04E-06
Ca K_α	1.08E-04	1.10E-04	-1.98E-04	3.49E-05	1.12E-03	1.75E-03	7.02E-04
Ti K_α	4.39E-05	4.73E-05	-6.68E-05	2.58E-05	5.79E-05	2.84E-04	6.60E-05
Mn K_α	2.27E-05	1.92E-05	-1.08E-05	1.25E-05	8.78E-05	1.03E-04	4.14E-05
Fe K_α	9.30E-04	9.43E-04	-1.96E-03	8.23E-04	4.69E-03	9.41E-03	2.90E-03
Co K_α	1.56E-05				7.33E-05		
Sr K_α	1.23E-05	1.19E-05	-2.14E-05	-3.28E-06	4.24E-06	2.79E-05	1.70E-06
Zr K_α	1.51E-05	9.13E-06	-1.44E-05	1.22E-05	2.26E-05	8.95E-06	1.40E-05

ation of the ten element sub-composition. The results indicate a satisfying homogeneity of the elements observed.

9.3 Comparison of calibration methods

To address the question if the log-ratio-calibration-equation (LRCE) method is gaining additional benefits compared to the “classic” calibration procedure, the standards were measured and both calibrations techniques applied. Therefore the model parameters α , β and goodness-of-fit statistics R^2 of the model I regression have been calculated. For reasons of comparison, the calculations have been carried out with the raw uncorrected data as well. The calculations were done for the Bruker AXS and the micro XRF setup to compare the differences of both configurations. In terms of the LRCE, all possible sub-compositions of the three parameters are given in Table 9.6 to 9.8.

In Table 9.4 the calculated model parameters of the raw micro XRF measurements are displayed. Naturally the goodness-of-fit statistic R^2 is poor for elements that are difficult to detect under atmospheric pressure like Al and Si. It is better for elements like Fe, K, and Ca which have a high signal to noise (S/N) ratio.

Regarding the intensity correction with the Compton scatter peak in Table 9.5, a better R^2 is yielded only for elements with poor correlation like Al and Co. The strong decrease in correlation for Si is discussed after the next page.

In Table 9.6, the model parameter α for the ten element sub-compositions

Table 9.3: Mean and standard deviation of each element of the 10 element sub-compositions of the USGS standards (see chapter 6).

		Al K_α	Si K_α	K K_α	Ca K_α	Ti K_α	Mn K_α	Fe K_α	Co K_α	Sr K_α	Zr K_α
RGM-1	mean	0.071	1.215	2.736	1.346	0.532	0.229	11.825	0.187	0.258	0.536
	st. dev.	0.007	0.068	0.149	0.075	0.032	0.017	0.692	0.021	0.026	0.033
QLO-1	mean	0.078	1.094	2.638	3.632	1.279	0.595	28.166	0.325	0.737	0.463
	st. dev.	0.008	0.062	0.135	0.190	0.071	0.036	1.452	0.030	0.045	0.033
SCo-1	mean	0.084	1.119	2.248	3.500	1.328	0.408	37.603	0.388	0.389	0.425
	st. dev.	0.008	0.052	0.108	0.177	0.073	0.025	1.754	0.031	0.027	0.032
SDC-1	mean	0.102	1.358	2.769	2.096	2.082	0.729	45.502	0.491	0.424	0.672
	st. dev.	0.011	0.070	0.182	0.110	0.142	0.057	2.564	0.037	0.032	0.078
DNC-1	mean	0.113	0.931	0.361	17.687	1.104	1.174	75.514	0.743	0.347	0.220
	st. dev.	0.013	0.069	0.030	1.195	0.105	0.085	4.958	0.060	0.033	0.029
W-2	mean	0.124	1.233	0.851	17.255	2.344	1.281	80.103	0.782	0.453	0.316
	st. dev.	0.014	0.077	0.060	1.059	0.173	0.089	5.057	0.061	0.041	0.032
BIR-1	mean	0.144	1.146	0.165	22.814	2.267	1.364	85.755	0.804	0.281	0.194
	st. dev.	0.014	0.067	0.015	1.304	0.141	0.086	4.893	0.061	0.028	0.025

Table 9.4: Model parameters α , β and goodness-of-fit statistics (R^2) of the raw, uncorrected micro XRF measurements. The asterisk (*) denotes missing data points of the indicated elements.

	Al	Si	K	Ca	Ti	Mn*	Fe	Co	Sr	Zr
α	-16.1	161.4	2588.4	4906.5	8530.2	18986.0	20792.2	161145.4	50974.9	63148.6
β	398.5	-1327.6	453.4	519.1	365.1	401.9	24863.3	890.2	194.6	239.8
R_2	0.113	0.775	0.967	0.978	0.908	0.974	0.924	0.707	0.852	0.926

Table 9.5: Model parameters α , β and goodness-of-fit statistics (R^2) of the Compton-corrected micro XRF measurements. The asterisk (*) denotes missing data points of the indicated elements.

	Al	Si	K	Ca	Ti	Mn*	Fe	Co	Sr	Zr
α	0.042	-0.015	0.748	2.916	3.157	12.440	14.026	154.678	17.980	14.565
β	-0.228	1.661	0.397	-1.535	0.313	-0.112	-10.004	0.187	0.128	0.215
R_2	0.626	0.154	0.959	0.887	0.743	0.721	0.763	0.894	0.687	0.872

are depicted. Note that the matrix of α is completely symmetrical. α can be regarded as the equivalent of the slope in the LRCE.

Table 9.6: Model parameter α calculated from the LRCE of the micro XRF measurements, for every possible sub-composition of the ten elements. The asterisk (*) denotes missing data points of the indicated elements.

	Al	Si	K	Ca	Ti	Mn*	Fe	Co	Sr	Zr
Al		1.111	0.716	0.946	0.715	0.783	0.786	0.256	1.170	0.611
Si	1.111		0.638	1.005	0.853	0.915	0.923	0.415	0.917	0.439
K	0.716	0.638		0.794	0.682	0.725	0.725	0.547	0.604	0.781
Ca	0.946	1.005	0.794		1.016	0.948	1.041	0.261	1.073	0.790
Ti	0.715	0.853	0.682	1.016		0.985	0.985	0.260	1.000	0.619
Mn	0.783	0.915	0.725	0.948	0.985		0.839	-0.147	1.027	0.689
Fe	0.786	0.923	0.725	1.041	0.985	0.839		-0.261	1.031	0.690
Co	0.256	0.415	0.547	0.261	0.260	-0.147	-0.261		0.472	0.444
Sr	1.170	0.917	0.604	1.073	1.000	1.027	1.031	0.472		0.467
Zr	0.611	0.439	0.781	0.790	0.619	0.689	0.690	0.444	0.467	

In Table 9.7, the model parameter β for the ten element sub-compositions are depicted. The matrix for β is symmetrical in the way that $A(\beta)=-C(\beta)$. β is regarded as the equivalent of the intercept in the LRCE.

Table 9.7: Model parameter β of the micro XRF measurements, calculated from the LRCE for every possible sub-composition of the ten elements. The asterisk (*) denotes missing data points of the indicated elements.

	Al	Si	K	Ca	Ti	Mn*	Fe	Co	Sr	Zr
Al		1.106	4.112	5.038	4.823	5.590	6.591	3.740	8.622	5.389
Si	-1.106		2.253	3.864	3.824	4.886	5.346	3.145	5.712	2.324
K	-4.112	-2.253		0.587	0.689	1.210	2.417	2.498	1.266	2.259
Ca	-5.038	-3.864	-0.587		0.628	1.329	1.623	-0.567	2.855	1.703
Ti	-4.823	-3.824	-0.689	-0.628		0.930	1.077	0.334	1.883	0.915
Mn	-5.590	-4.886	-1.210	-1.329	-0.930		0.751	-0.896	0.979	0.743
Fe	-6.591	-5.346	-2.417	-1.623	-1.077	-0.751		-6.566	1.011	-0.611
Co	-3.740	-3.145	-2.498	0.567	-0.334	0.896	6.566		-1.277	-1.058
Sr	-8.622	-5.712	-1.266	-2.855	-1.883	-0.979	-1.011	1.277		0.166
Zr	-5.389	-2.324	-2.259	-1.703	-0.915	-0.743	0.611	1.058	-0.166	

A closer look on Table 9.8 reveals, that the log ratio with K as common denominator yields the best over all performance of all 10 observed elements. The log ratio with Ca performs a bit better sometimes, but fails completely with element Co. Therefore the potassium values will be taken as representatives for the LRCE-method when comparing the calibrations.

The comparison of the three data sets of R^2 values (raw, corrected and LRCE) is displayed in figure 9.4. The first column denotes the values without

Table 9.8: Goodness-of-fit statistics R^2 of the micro XRF measurements, calculated from the LRCE for every possible sub-composition of the ten elements. The asterisk (*) denotes missing data points of the indicated elements.

	Al	Si	K	Ca	Ti	Mn*	Fe	Co	Sr	Zr
Al		0.902	0.989	0.991	0.885	0.937	0.933	0.937	0.857	0.930
Si	0.902		0.986	0.998	0.982	0.978	0.988	0.989	0.906	0.912
K	0.989	0.986		0.988	0.988	0.982	0.983	0.993	0.970	0.950
Ca	0.991	0.998	0.988		0.988	0.976	0.979	0.055	0.995	0.977
Ti	0.885	0.982	0.988	0.988		0.984	0.991	0.532	0.992	0.912
Mn	0.937	0.978	0.982	0.976	0.984		0.929	0.283	0.982	0.951
Fe	0.933	0.988	0.983	0.979	0.991	0.929		0.767	0.996	0.948
Co	0.937	0.989	0.993	0.055	0.532	0.283	0.767		0.926	0.984
Sr	0.857	0.906	0.970	0.995	0.992	0.982	0.996	0.926		0.766
Zr	0.930	0.912	0.950	0.977	0.912	0.951	0.948	0.984	0.766	

any calibration (raw). The second column represents the classic method where the Compton scatter peak is used. The last column depicts the values of the LRCE when K is used as common denominator.

An obvious first result is that the classic Compton peak correction method fails completely for this sample. The correlation is throughout far worse than the uncorrected data and the LRCE data. Especially Si stands out as a negative example. Several reasons are responsible for the odd behavior of the Si correlation. First of all, the Si K_{α} radiation is absorbed by the air path between sample and detector and the Be entrance window, limiting the accessible energy range to photons greater than approximately 2 keV (see also *R. Van Grieken* in [9] chapter 3).

Secondly it is the main component in the standards, thus one has to correlate the low intensity with high weight-percentage. Finally the standards have only two levels of Si by coincidence: Four standards contain around 70 % SiO₂ and three have around 50 %. This leads to strong decrease in R^2 when the classic calibration method is applied. The use of the LRCE is able to overcome this issues, resulting in a major increase in correlation (> 0.98).

Though maybe not directly visible, the correlation is always slightly better with the LRCE (K). The information about K is lost in the LRCE (K) since it is used as common denominator.

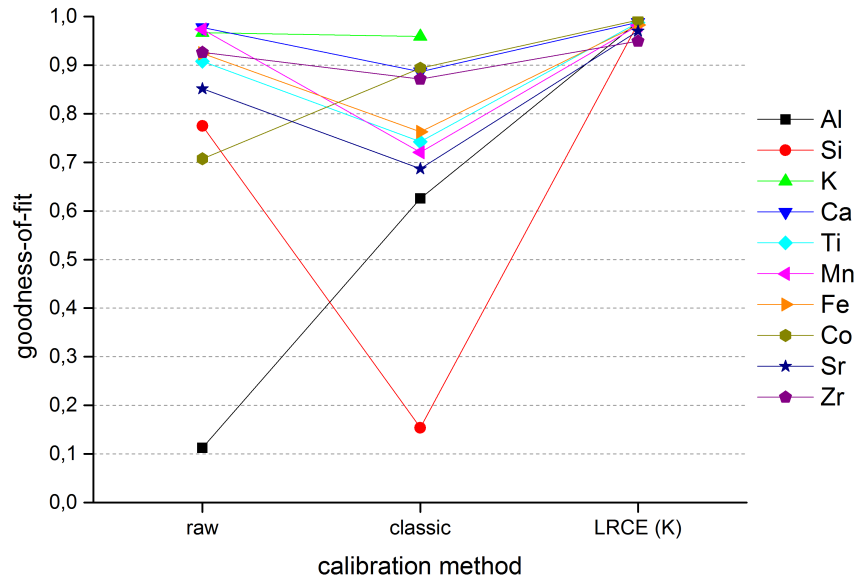


Figure 9.4: Comparison of the different calibration methods in terms of goodness-of-fit. Displayed values are for the micro XRF setup.

9.4 Geological sample

The geological sample contained mainly Ca, and in minor concentrations K, Fe, Sr, and Zr. The results for the line scans are given separately for each element, comparing the raw calibration, with the Compton peak corrected one and the LRCE for potassium. The setup was already shown in Figure 3.2 on page 36. The scan was carried out vertically from the bottom to the top. The distinct peak around measurement number 65 is due to a cavity in the sample surface. It can be observed as darker spot on the sample surface in Figure 3.2. To give a statement which of the calibrations worked best, measurements with at least one independent analytical method have to be carried out. A neutron activation analysis (NAA) would be suitable for this task. The sample composition was unfortunately quite different to the used standards and was thus outside the optimal range of the calibration curve. This leads to larger errors. In case of Fe, the calibration of the raw data failed completely since it resulted in a negative weight percentage.

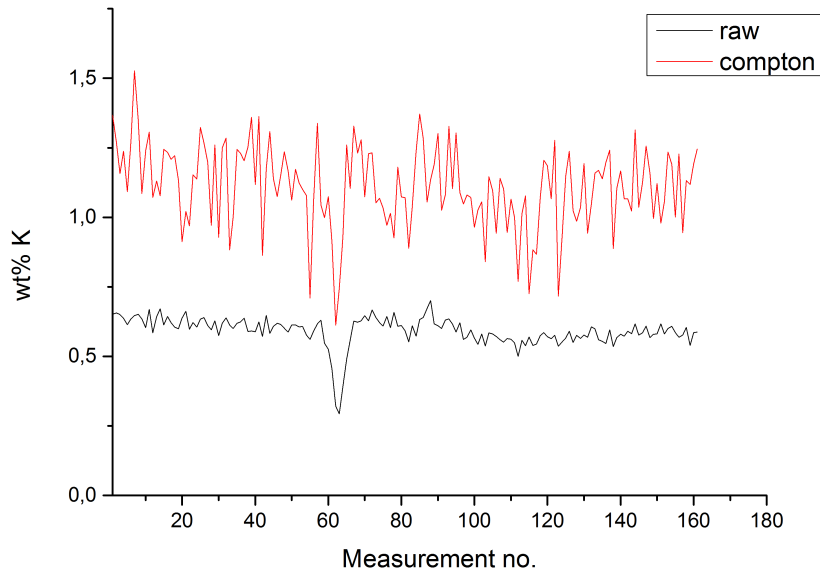


Figure 9.5: Results for K; The data is presented in wt % K.

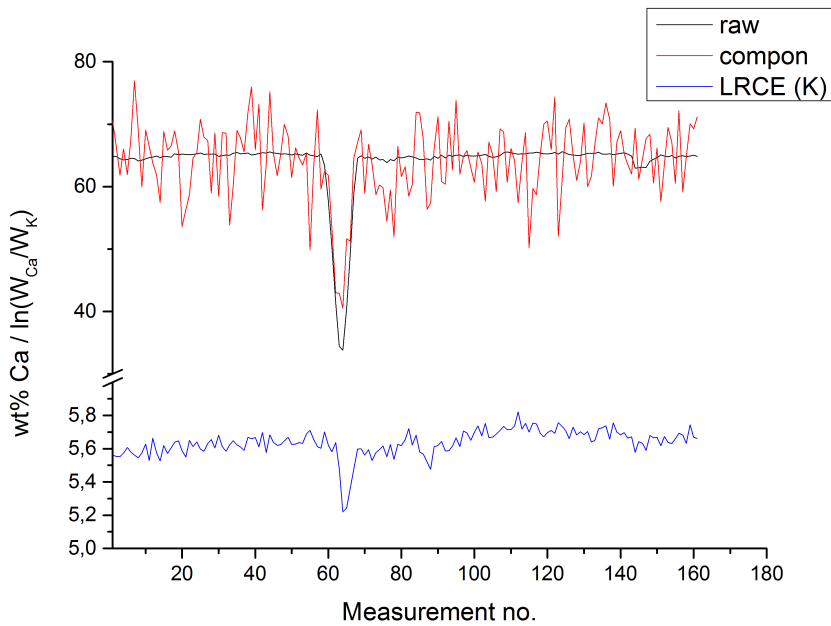


Figure 9.6: Results for Ca; The raw and Compton corrected data is presented in wt % Ca, while the LRCE data is denoted in the dimensionless log-ratio unit.

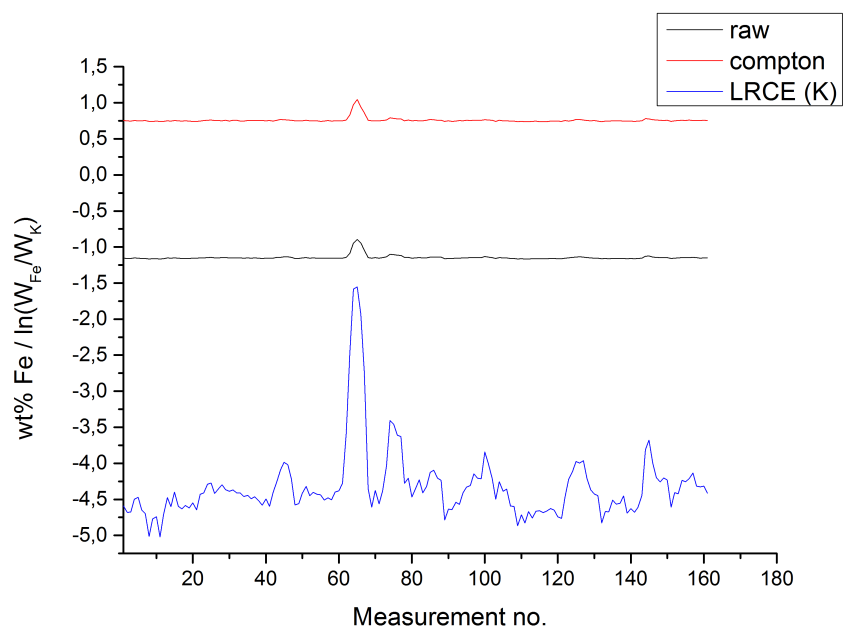


Figure 9.7: Results for Fe; The raw and Compton corrected data is presented in wt % Fe, while the LRCE data is denoted in the dimensionless log-ratio unit. The Fe content of the sample is to far outside the analytical meaningful range of the calibration, since a negative Fe content is obtained.

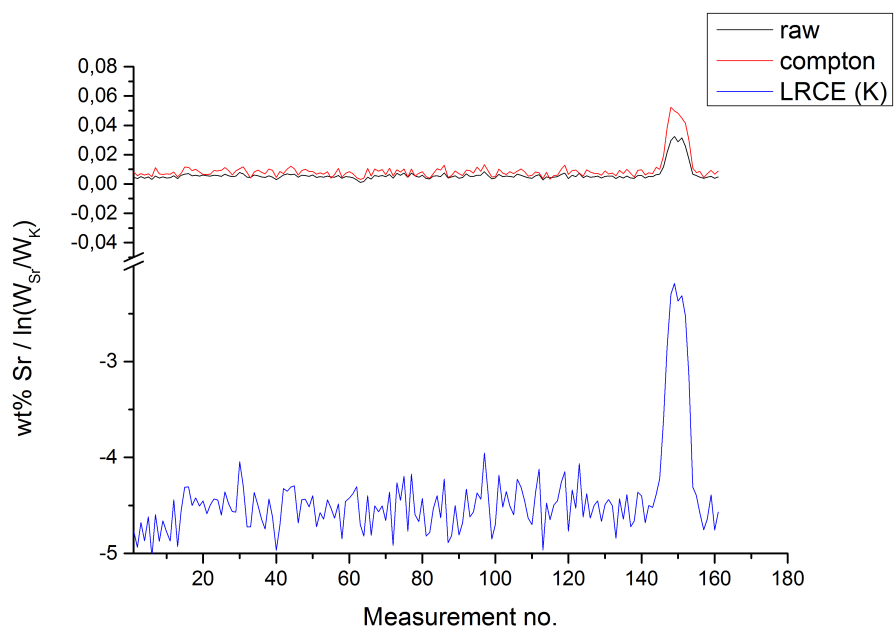


Figure 9.8: Results for Sr; The raw and Compton corrected data is presented in wt% Sr, while the LRCE data is denoted in the dimensionless log-ratio unit.

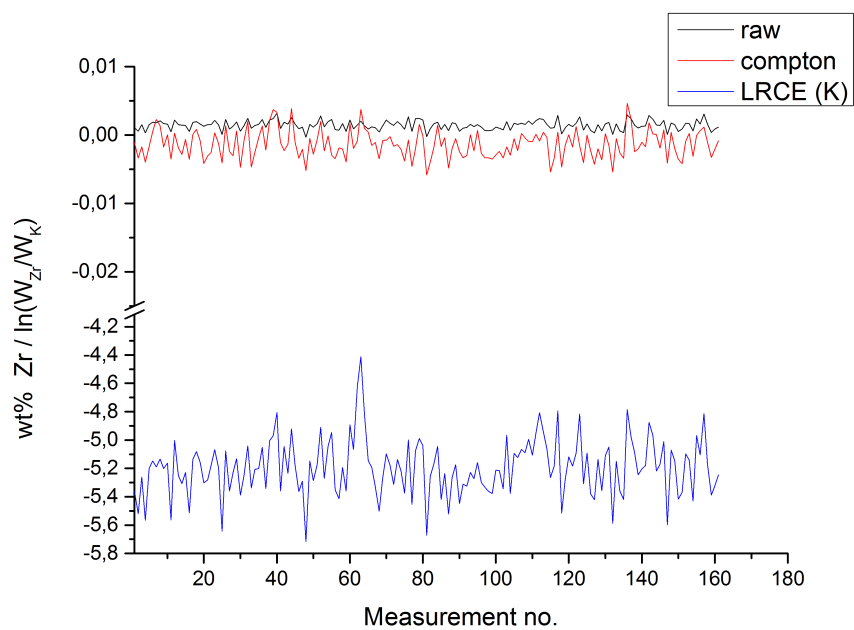


Figure 9.9: Results for Zr; The raw and Compton corrected data is presented in wt% Zr, while the LRCE data is denoted in the dimensionless log-ratio unit.

Chapter 10

Hand-held XRF

The comparison of the calibration methods were also carried out on a commercially available hand held device to compare the results to the laboratory setup. An opportunity occurred during my time at the UA Antwerp to carry out measurements in the royal gardens in Brussels as a part of an restoration project. The data might be unrelated to the goal of the thesis, but will be mentioned here so that the information is not lost. Data and results of these measurements are given in section 10.2.

The measured Co intensity is very low and at some standards not measurable with the hand-held device or even with the micro XRF setup. This leads to very poor results where Co signals are involved. In the LRCE the calculations of the Co signal is completely absent, due to the missing Co data. In the Mn-dataset is one data point missing and in the Zr-dataset there are two data points missing because they were not detectable. The elements where one or more data points are missing are indicated with an asterisk(*) in the upcoming tables. The difference is neglectable though, since the R^2 value changes hardly at all ($R = \pm 0.001$).

10.1 Comparison of calibration methods

In Table 10.1 the calculated model parameters α , β and the goodness-of-fit statistics R^2 of the raw, uncorrected Bruker Tracer III-V⁺ XRF measurements are given.

Table 10.2 depicts the calculated model parameters α , β and goodness-of-fit statistics R^2 of the Compton peak corrected Bruker Tracer III-V⁺ XRF measurements. As mentioned above, the negative slope and thus the complete lack of correlation is visible for the Co measurement. The quality of the intercept values are a major step forward, when the correction is applied.

A perfect correlation would have to pass the origin in order to be applicable to a wide range of concentrations. The more the calibration curve

Table 10.1: Model parameters α , β and goodness-of-fit statistics R^2 of the raw, uncorrected Bruker Tracer III-V⁺ XRF measurements.

	Al	Si	K	Ca	Ti	Mn*	Fe	Sr	Zr*
α	37.8	3599.6	15776.7	20515.6	27326.7	74658.8	82657.0	451192.6	476583.3
β	5133.8	-54133.0	-1193.7	6566.0	5821.3	2773.3	246670.6	-632.3	-713.5
R^2	0.003	0.932	0.980	0.996	0.640	0.946	0.919	0.821	0.677

lacks this condition the narrower is its field of application and the bigger the error, when measured outside of this optimal range.

Table 10.2: Model parameters α , β and goodness-of-fit statistics R^2 of the Compton peak corrected Bruker Tracer III-V⁺ XRF measurements.

	Al	Si	K	Ca	Ti	Mn*	Fe	Sr	Zr*
α	0.039	0.038	0.470	1.229	1.923	5.464	6.388	15.289	16.899
β	-0.085	0.743	0.091	-0.516	-0.058	-0.034	-1.176	0.024	-0.034
R^2	0.432	0.645	0.973	0.994	0.989	0.985	0.995	0.995	0.975

In Table 10.3 the model parameter α is calculated from the LRCE of the Bruker Tracer III-V⁺ XRF measurements for every possible sub-composition of the ten elements.

Table 10.3: Model parameter α calculated from the LRCE of the Bruker Tracer III-V⁺ XRF measurements for every possible sub-composition of the ten elements. The asterisk (*) denotes missing data points of the indicated elements.

	Al	Si	K	Ca	Ti	Mn*	Fe	Sr	Zr*
Al		1.213	0.827	1.009	0.837	0.819	0.822	1.082	1.423
Si	1.213		0.758	1.074	0.874	0.957	0.955	0.858	1.167
K	0.827	0.758		0.897	0.767	0.830	0.819	0.734	0.500
Ca	1.009	1.074	0.897		1.121	0.970	1.067	1.118	1.134
Ti	0.837	0.874	0.767	1.121		1.228	1.177	0.983	1.101
Mn	0.819	0.957	0.830	0.970	1.228		0.981	1.087	1.155
Fe	0.822	0.955	0.819	1.067	1.177	0.981		1.026	1.126
Sr	1.082	0.858	0.734	1.118	0.983	1.087	1.026		1.041
Zr	1.423	1.167	0.500	1.134	1.101	1.155	1.126	1.041	

Table 10.4 depicts the model parameter β calculated from the LRCE of the Bruker Tracer III-V⁺ XRF measurements for every possible sub-composition of the ten elements. A closer look reveals that the element with the best performance is again potassium (as denominator). Never-

theless the intercept values of the LRCE are worse than the ones with the Compton correction.

Table 10.4: Model parameter β calculated from the LRCE of the Bruker Tracer III-V⁺ XRF measurements for every possible sub-composition of the ten elements. The asterisk (*) denotes missing data points of the indicated elements.

	Al	Si	K	Ca	Ti	Mn*	Fe	Sr	Zr*
Al		0.604	2.796	3.580	3.659	4.322	5.269	6.919	8.936
Si	-0.604		1.481	2.874	2.759	4.070	4.440	4.494	6.705
K	-2.796	-1.481		0.507	0.793	1.576	2.490	2.182	0.970
Ca	-3.580	-2.874	-0.507		0.828	1.473	1.789	3.449	3.432
Ti	-3.659	-2.759	-0.793	-0.828		1.409	0.806	2.198	2.438
Mn	-4.322	-4.070	-1.576	-1.473	-1.409		0.285	1.375	1.353
Fe	-5.269	-4.440	-2.490	-1.789	-0.806	-0.285		1.167	1.593
Sr	-6.919	-4.494	-2.182	-3.449	-2.198	-1.375	-1.167		-0.090
Zr	-8.936	-6.705	-0.970	-3.432	-2.438	-1.353	-1.593	0.090	

In Table 10.5 the goodness-of-fit statistics calculated from the LRCE of the Bruker Tracer III-V⁺ XRF measurements are depicted for every possible sub-composition of the ten elements. It comes at no surprise that the correlation with potassium as denominator performs well, considering the performance with the micro XRF setup. Again it has the highest overall correlation. The comparison of the three data sets (raw, corrected and LRCE) are displayed in figure 10.1.

Table 10.5: Goodness-of-fit statistics (R^2) calculated from the LRCE of the Bruker Tracer III-V⁺ XRF measurements for every possible sub-composition of the ten elements. The asterisk (*) denotes missing data points of the indicated elements.

	Al	Si	K	Ca	Ti	Mn*	Fe	Sr	Zr*
Al		0.946	0.990	0.990	0.872	0.977	0.971	0.874	0.917
Si	0.946		0.990	0.993	0.978	0.983	0.988	0.928	0.751
K	0.990	0.990		0.991	0.994	0.988	0.989	0.985	0.930
Ca	0.990	0.993	0.991		0.965	0.937	0.933	0.986	0.973
Ti	0.872	0.978	0.994	0.965		0.974	0.989	0.978	0.983
Mn	0.977	0.983	0.988	0.937	0.974		0.906	0.992	0.998
Fe	0.971	0.988	0.989	0.933	0.989	0.906		0.997	0.995
Sr	0.874	0.928	0.985	0.986	0.978	0.992	0.997		0.978
Zr	0.917	0.751	0.930	0.973	0.983	0.998	0.995	0.978	

Figure 10.1 displays the calculated R^2 values when different calibration methods are applied. Elements that have little to no correlation in the “raw” data like Al, Ti, and Zr benefit most from the classic calibration.

Application of the LRCE with K as denominator leads to a major increase for the Al correlation. Over all the Al data profits th most from the LRCE. For Elements Fe, Sr, Zr, and Ti, the classic calibration method is superior. The LRCE is quite close to these values though. The strange behavior of Si has already been discussed in the previous chapter. The LRCE is here distinctively better than both other data sets.

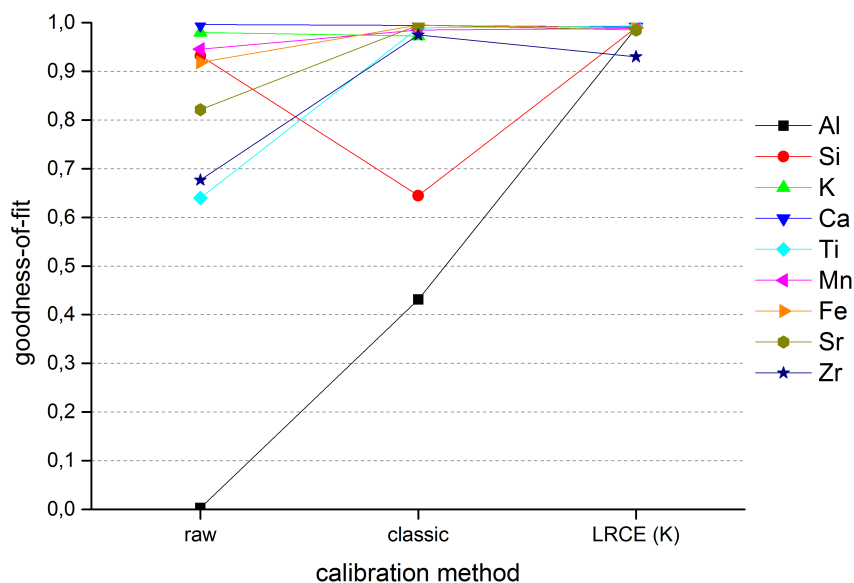


Figure 10.1: Comparison of the different calibration methods in terms of goodness-of-fit. Values for the hand-held Bruker Tracer III-V are shown. The information of K is lost in the process of the LRCE calibration. Especially for elements with poor correlation, major improvements are observed, when the LRCE is applied.

10.2 Japanese tower in Brussels

In May 2013, during my Erasmus stay in Antwerp, I had the opportunity to join the team of Dr. Jana Sanyova of the Royal Institute for Cultural Heritage (KIK-IPRA) for a week. Their team worked on a restoration project in the Japanese tower in the royal gardens of Brussels. The task was to record XRF spectra of different spots of interest in the tower with the hand-held XRF device. The goal was to evaluate the qualitative composition of the sample spots. A quantitative evaluation proved to be not possible in regard to the

undefined sample geometries, the poorly defined matrices and the lack of available standards.

The four samples labeled as paper matrices in Table 10.7 on page 85 are old wallpapers in the staircase of the tower. By far the highest intensity stems from zinc. ZnO is used as paper coating and as a white pigment. Another intense signal is lead. It most probably stems from the compound white lead ($2\text{PbCO}_3 \cdot \text{Pb(OH)}_2$), a historic art paint. Other elements present in higher concentrations are Sulfur, calcium, iron and tin resp. strontium in sample 34.

The data from the four spectra in Table 10.8 on page 86 was recorded from a wooden column in the fourth floor of the tower. They depict a carved eagle that was gilded. Figures 10.2 a and 10.2 b on page 87 show the setup on site.

From the specific elements detected, the conclusion can be drawn that the so called water gilding was applied. This technique is used for the gilding of wood. First a coat of rabbitskin-glue and calcit/gypsum [41] (CaSO_4), the “gesso” is applied on the wood. Afterwards a layer of clay mixture (Armenian clay, reddish color due to presence of iron oxide (Fe_2O_3)) is added. Water is applied to the surface to make it sticky. Immediately after that gold (Au) is applied. Sample spots 10, 11 and 13 had a golden color, while 12 had a dark grey-bluish color. An intense gold peak was recorded in spectrum 10 and 11, a smaller but still distinct one in spectrum 21 and 13. The source of mercury in all samples and arsenic in sample 12 could not be determined.

The spectra recorded from the glass ornament are given in Table 10.9 on page 89. Sample 14 and 41 are yellow. A distinct amount of silver was only found in the two samples, which indicates a coloration with Silver (so called silveryyellow). Another yellow color is created when mixing iron oxide and manganese oxide (MnO_4) in absence of sulfur. An increased amount of iron, manganese and a significant lower amount of sulfur was found in the two samples suggesting that these elements are also involved in the coloring. An unambiguous assignment for the elements responsible for color in samples 37, 38, 39 and 40 was not possible.

As expected from brass, the two main components are copper and zinc. The third component that stands out is lead. In brass alloys it is used to increase strength and workability. Figure 10.3 displays the setup for the measurement of the brass handle in on the door in the first floor of the tower.

Table 10.6: *Samples measured in the japanese tower in the royal gardens of Brussels. The names give indication of the measurement conditions and the position in the tower. On the right side the different matrices are shown.*

sample name	glass	paper	metall	wood
01 25 kV 2 μ A Jap Tower 1st floor ceiling 250s			x	
02 25 kV 2 μ A Jap Tower 1st varnish green lamp #2 250s			x	
03 25 kV 2 μ A Jap Tower 1st varnish green lamp 250s			x	
04 25 kV 2A Jap Tower 4 fl high black flower pillow 250s			x	
05 25 kV 2 μ A Jap Tower 4 fl high gold flower pillow 250s			x	
06 25 kV 2 μ A Jap Tower original cleaned gilding 250s			x	
07 25 kV 2 μ A Jap Tower original cleaned gilding bottom 250s			x	
08 25 kV 2 μ A Jap Tower original cleaned gilding double layer 250s			x	
09 25 kV 4 μ A Jap Tower 4 fl Column gold gilding 250s			x	
10 25 kV 8 μ A Jap Tower 4 fl Column eagle face gold 250s				x
11 25 kV 8 μ A Jap Tower 4 fl Column eagle feather lightgold 250s				x
12 25 kV 8 μ A Jap Tower 4 fl crane blue leaf 250s				x
13 25 kV 8 μ A Jap Tower 4 fl golden waves 250s				x
14 25 kV 10 μ A Jap Tower 3rd fl light yellow glass 500s	x			
15 25kV 2 μ A Jap Tower 1st fl column west black 500s			x	
16 25kV 2 μ A Jap Tower 1st fl column west gold 500s			x	
17 25kV 2 μ A Jap Tower 1st fl door west			x	
18 25kV 2 μ A Jap Tower 1st fl Stairs green door brasspowder			x*	
19 25kV 2 μ A Jap Tower 1st fl varnish green lamp 250s			x	
20 25kV 2 μ A Jap Tower 3rd fl #1			x	
21 25kV 2 μ A Jap Tower 3rd fl #2			x	
22 25kV 2 μ A Jap Tower 3rd fl column black_gold#2			x	
23 25kV 2 μ A Jap Tower 3rd fl door west gold			x	
24 25kV 3 μ A Bat_wing 250s			x	
25 25kV 3 μ A Butterfly_wing 250s			x	
26 25kV 3 μ A Jap Mask patina 250s #2			x	
27 25kV 3 μ A Jap Mask patina 250s			x	
28 25kV 4 μ A Jap Tower 3rd fl door lintel #1			x	
29 25kV 4 μ A Jap Tower 3rd fl door lintel #2			x	
30 25kV 4 μ A Jap Tower 3rd fl door lintel #3			x	
31 25kV 4 μ A Jap Tower 3rd fl door stairs gold handle #2			x	
32 25kV 4 μ A Jap Tower wallpaper white 250s		x		
33 25kV 8 μ A Jap Tower 3rd fl door stairs gold handle #1			x	
34 25kV 8 μ A Jap Tower wallpaper brown 250s		x		
35 25kV 8 μ A Jap Tower wallpaper gold 250s		x		
36 25kV 10 μ A Jap Tower wallpaper paper250s		x		
37 35 kV 2 μ A Jap Tower 3rd fl blue bird glass 500s	x			
38 35 kV 2 μ A Jap Tower 3rd fl leafe green glass 500s	x			
39 35 kV 2 μ A Jap Tower 3rd fl red birdhead glass 500s	x			
40 35 kV 2 μ A Jap Tower 3rd fl treegrey glass 500s	x			
41 35 kV 10 μ A Jap Tower 3rd fl dark yellow glass 500s	x			
42 40kV 2 μ A Jap Tower 1st fl Stairs green door brasspowder 250s				x*

* although Brass is a categorized as metal matrix it will be addressed in a separate table.

Table 10.7: *The four measurements carried out on a paper matrix. The columns indicate the sample number, while the rows give the element intensity and the corresponding standard deviation below.*

Spectrum	32	34	35	36
S K_α	24253	30666	6764	7446
std. dev.	175	217	151	109
K K_α				8764
std. dev.				126
Ca K_α	29678	40934	170747	21340
std. dev.	183	418	426	166
Ti K_α	302		2857	5680
std. dev.	63		120	112
V K_α	330	1019		2672
std. dev.	65	99		109
Cr K_α	3357	1607	1292	
std. dev.	91	109	107	
Mn K_α	209	1335	714	2470
std. dev.	80	121	117	127
Fe K_α	13578	80184	34340	102792
std. dev.	147	309	227	343
Co K_α			759	
std. dev.			153	
Ni K_α	1095			
std. dev.	109			
Cu K_α	2855	7601	4923	5099
std. dev.	137	180	178	172
Zn K_α	981311	10922	735155	113863
std. dev.	950	198	837	378
Ga K_α	6517		7694	
std. dev.	167		187	
Sr K_α		11442		
std. dev.		211		
Sn-La		179103		
std. dev.		470		
Pb-La	42905	23935	15978	487274
std. dev.	176	242	138	528

Table 10.8: *Measurements carried out on a wooden matrix. The columns indicate the sample number, while the rows give the element intensity and below the corresponding standard deviation.*

Spectrum	10	11	12	13
S K_α	69847	99938	20189	63098
std. dev.	311	345	207	277
K K_α		1845	18436	
std. dev.		126	205	
Ca K_α	30987	139896	258396	75667
std. dev.	202	375	510	282
Ti K_α	507	1772	2624	1125
std. dev.	82	93	124	90
Mn K_α	2544	2297	5435	2915
std. dev.	128	123	142	130
Fe K_α	143027	164842	350786	312568
std. dev.	398	417	588	558
Cu K_α	13427	10229	9831	132053
std. dev.	199	184	173	392
Zn K_α		6824	5004	22656
std. dev.		215	165	245
As K_α			78160	6619
std. dev.			339	203
Sr K_α			4656	
std. dev.			208	
Au-La	134836	27608	6236	2109
std. dev.	385	267	152	196
Hg-La	270663	247808	14542	226866
std. dev.	479	444	191	399

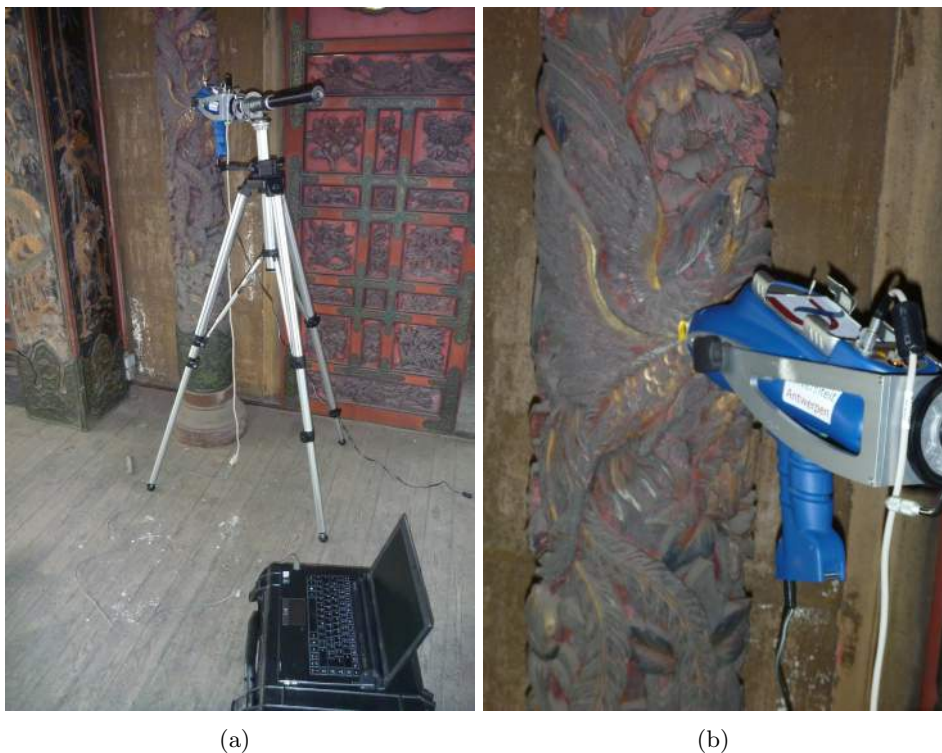


Figure 10.2: Setup for the measurement of the wooden column in the fourth floor. The dark red color probably stems from Fe_2O_3 in Armenian clay, that is used during gilding. The gold layer can also be seen in the better preserved cavities and narrow gaps. (a) overview, (b) detail.

Table 10.11 on page 91 gives an overview about the elements found in the miscellaneous metal samples measured at the Japanese tower. Each row is a sample, while the columns give the element intensity and the standard deviation.

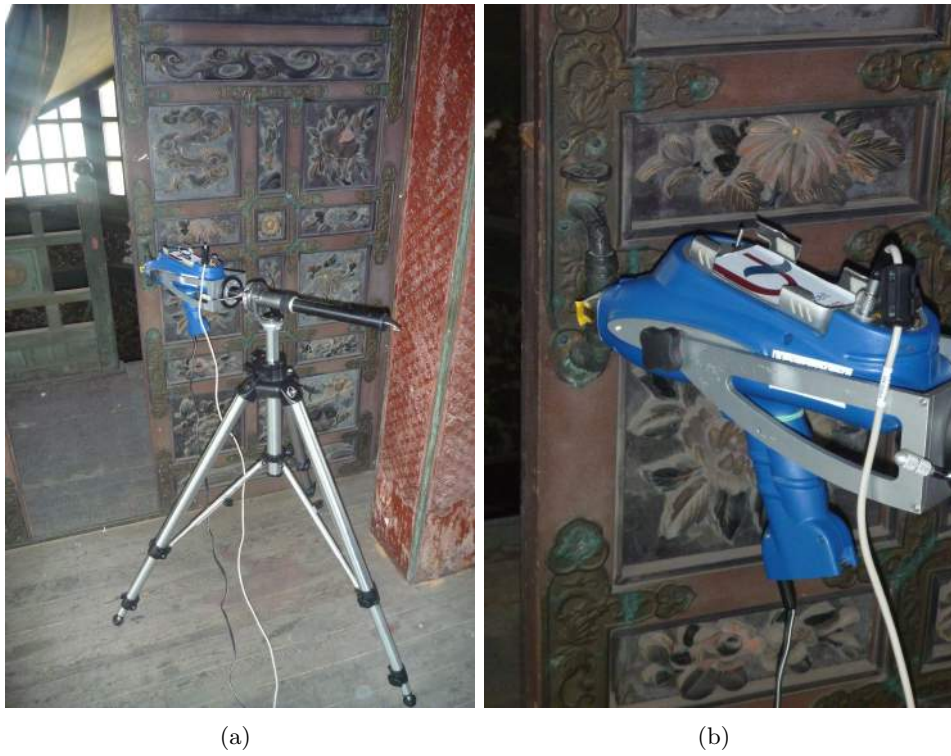


Figure 10.3: *Setup for the measurement of the brass handle in the first floor. (a) overview, (b) detail.*

Table 10.9: *Measurements carried out on a glass matrix. The samples are different spots from the glass ornaments in the main door of the third floor. The columns indicate the sample number, while the rows give the element intensity and below the corresponding standard deviation.*

Spectrum	14	37	38	39	40	41
Si K_α	148178	3679	3616	6217	2459	207963
std. dev.	415	124	119	135	99	486
S K_α	1731	140300	107583	127584	69643	6804
std. dev.	142	392	347	376	375	182
K K_α	7621					18461
std. dev.	233					234
Ca K_α	386167	1885	3515	12484	3623	485408
std. dev.	616	86	97	138	91	688
Ti K_α	1410	556	637	449	994	1817
std. dev.	131	75	75	76	70	144
Cr K_α		2269	4593	28107	1567	
std. dev.		106	116	194	91	
Mn K_α	2893					3971
std. dev.	181					200
Fe K_α	29584	3277	15811	19668	43179	41357
std. dev.	266	135	177	187	233	296
Co K_α		3585	2236			
std. dev.		153	149			
Ni K_α	2190	2464	1492	1986	1535	1611
std. dev.	278	157	152	149	135	254
Cu K_α	19231	6300	37992	15474	18299	24715
std. dev.	286	191	268	208	205	309
Zn K_α	4831	551107	510804	195130	332177	5516
std. dev.	272	745	721	472	586	288
Sr K_α	9209					10278
std. dev.	353					371
Zr K_α	3820					5893
std. dev.	345					361
Ag K_α	14403					21558
std. dev.	320					343
Sn K_α		3066	3269	4285	2921	
std. dev.		105	104	130	106	
Au-La	2577					2570
std. dev.	293					247
Pb-La	13241	1144963	1089790	1114131	1017984	15803
std. dev.	262	779	758	768	732	278

Table 10.10: *The two samples taken from a brass door handle in the first floor of the tower. Each column indicates a sample, while the rows give the element intensity and below the corresponding standard deviation.*

spectrum	18	42
S K_α	20541	12043
std. dev.	160	130
Ti K_α	8733	6083
std. dev.	123	107
Mn K_α	1192	725
std. dev.	106	94
Fe K_α	42068	29498
std. dev.	243	205
Ni K_α	1922	2141
std. dev.	147	138
Cu K_α	1027113	778991
std. dev.	1034	905
Zn K_α	117787	90086
std. dev.	411	378
Sr K_α	1853	3247
std. dev.	113	117
Sn-La	4250	2708
std. dev.	110	102
Pb-La	209730	256040
std. dev.	472	514

Table 10.11: *The elements found in the metal samples are given. Each row indicates a sample, while the columns give the element intensity and the standard deviation subsequently. First the intensity in counts is given, in the subsequent column the standard deviation is depicted.*

#	S K_{α}		Ca K_{α}		Ti K_{α}		Cr K_{α}		Fe K_{α}		Co K_{α}		Ni K_{α}		Cu K_{α}		Zn K_{α}		Au-La		Hg-La		Pb-La		
1	8115	119	230	40									2049	119	1462017	1220	9853	190	5933	99					
2	7039	109	1134	49	690	47			5026	107					815112	881	450086	672						1076	45
3	5968	100	757	43	230	40	254	49	3606	93			591	92	556128	728	330121	574						1451	62
4	667	47	542	40			447	48	16317	149					707623	856	370938	661						1560	60
5	1788	70	1502	59	176	44	202	57	8993	133					1015086	1023	534891	797						1070	45
6	614	45	274	45					105	110			7700	155	1422526	1136	12542	186	5554	110	1018	75	918	67	
7	947	51	269	42					956	95	916	93	3490	122	1395826	1159	10770	178	5644	76	827	52	1050	48	
8	2150	65	247	44	114	43	250	60	582	95			3544	124	1379684	1119	9783	178	12822	141	2549	89	1294	70	
9	5027	90	564	50	257	49	1034	67	2855	105			2566	111	1408693	1126	13879	177	8025	86					
15	14270	138	2267	82					3829	151			5160	170	2970072	1637	26817	258	8749	148	2869	109	6398	117	
16	16731	174	5870	104	961	74			14578	185					2936656	1726	26503	277	8271	133	2376	108	5973	114	
17	7037	120	301	46					668	113					1396445	1126	14886	196	12364	141	575	76	399	63	
19	5973	100	758	43	251	39	254	49	3606	93			591	92	556134	728	330113	574						1319	44
20	11605	147	1494	67	600	61	1089	78	5268	128					2015943	1350	21249	220	4763	115	697	76	1578	79	
21	14692	162	1475	69	381	64	1201	84	5890	141	1433	148			2616414	1535	25705	236	3848	117	815	86	2122	89	
22	14046	157	869	60	699	65	1179	86	4064	136			4220	146	2600422	1530	22497	230	6346	130	2270	97	1794	87	
23	10043	147	1359	74			830	85	4981	144	2071	128			2829731	1597	25007	243	7982	138	786	91	2650	95	
24	6012	103	1404	55	282	47	1048	65	12663	144					1007263	972	259121	528						8014	111
25	3564	87	2212	68					12548	148					1059072	1044	355440	662						4193	93
26	8737	126	1410	60			453	70	17786	171					1178656	1056	425446	708						3074	85
27	7480	118	1476	61	297	52	586	69	16270	163					1094902	1063	426601	722						2454	81
28	8250	117	295	48					4322	123					1074774	1022	616328	846	2260	225				2302	91
29	8266	108	422	53	402	57			5052	127					1095408	1036	583590	835	3004	250				2520	91
30	7076	96	323	42	275	47			3976	108			1878	115	905330	965	468122	722	3730	149				2110	72
31	8872	129	3325	77	994	61			13470	152					930614	980	328175	635	26220	293	1221	109	1634	93	
33	10441	126	4287	96	1400	76			17263	178					1130098	1092	407832	730	31337	333	411	143	2003	115	

Chapter 11

Conclusions

The long time drift test of the micro XRF setup revealed that the Fe K_α peak, the strongest signal by far, shows a drift behavior in the first few measurements. Elements K and Ca decrease only a bit, nevertheless they contribute to the overall trend. Since the Rh scatter peak decreases in intensity as well, the correction with the incoherent Compton peak eradicates this error. The drop in intensity at the beginning may stem from the “cold” start of the x-ray tube.

The homogeneity of the prepared standards proved to be satisfying showing hardly any change in intensity for the 10 elements sub-composition.

The following conclusions can be drawn for the comparison of the calibration methods with the micro XRF setup:

The calculated slope α of the calibration methods shows that the LRCE(K) is more sensitive to elements difficult to measure like Al and Si. For the other elements in the sub-composition the Compton corrected measurements are way more sensitive.

Regarding the y-intercept β , a low value is better, since the ideal linear calibration line is passing the origin. Except for Fe and Ca, the Compton correction method yields a better (thus smaller) intercept. Especially for small intensities the error increases strongly, leading to negative weight percentages (positive intercept) or to wrong positives (negative intercept).

The coefficient of determination R^2 was calculated under the assumption of a solely linear dependence. The data shows that the LRCE(K) is clearly superior to the Compton correction method, thus gaining a higher correlation. Surprisingly the raw correlation is also better than the Compton correction method.

The unknown geological sample has been analyzed, but a verification demands an alternative method for comparison in order to draw conclusions about the correctness of the calculated values.

The hand-held measurements are consistent with the α and β data of the micro XRF when it comes to the comparison of the calibration methods.

The goodness-of-fit R^2 however shows a somewhat other picture: Elements that suffer from strong absorption in air (Al, Si) or low count rate (Al, Mn) benefit from the LRCE (K) thus improving the goodness-of-fit. For elements Ti, Fe, Sr, and Zr that are well detectable under atmospheric pressure the Compton peak correction is slightly better than the LRCE (K). A look on Ca reveals that the raw data performs best, having an already excellent fit.

Distinct statements for the measurements in the Japanese tower in Brussels are hard to archive. For the wallpaper samples, the white paint was identified safely. The wooden pillars that were gilded supported the conclusion that the so called water-gilding method was utilized. Regarding the glass ornaments, only the yellow color could be determined with enough confidence. The other colors remained unknown. Finally, within the metal samples, the brass could be identified effortlessly.

Bibliography

- [1] W.C. Röntgen. *Eine neue Art von Strahlen*. Verlag und Druck der Stahel'schen K. Hof- und Universitäts-Buch- und Kunsthandlung, 1896.
- [2] H.G.J. Moseley. The high-frequency spectra of the elements part ii. *Philosophical Magazine Series 6*, 27(160):703–713, 1914.
- [3] H. Friedman and L. S. Birks. A geiger counter spectrometer for x-ray fluorescence analysis. *Review of Scientific Instruments*, 19(5):323–330, 1948.
- [4] P. E. Clark and B. R. Hawke. Compositional variation in the Hadley Apennine region. In R. B. Merrill and R. Ridings, editors, *Lunar and Planetary Science Conference Proceedings*, volume 12 of *Lunar and Planetary Science Conference Proceedings*, pages 727–749, 1982.
- [5] R. Guy Rothwell, Babette Hoogakker, John Thomson, Ian W. Croudace, and Michael Frenz. Turbidite emplacement on the southern balearic abyssal plain (western mediterranean sea) during marine isotope stages: an application of itrax xrf scanning of sediment cores to lithostratigraphic analysis. *Geological Society, London, Special Publications*, 267(1):79–98, 2006.
- [6] J. Thomson, I. W. Croudace, and R. G. Rothwell. A geochemical application of the itrax scanner to a sediment core containing eastern mediterranean sapropel units. *Geological Society, London, Special Publications*, 267(1):65–77, 2006.
- [7] Gert Jan Weltje and Rik Tjallingii. Calibration of xrf core scanners for quantitative geochemical logging of sediment cores: Theory and application. *Earth and Planetary Science Letters*, 274:423 – 438, 2008.
- [8] G.J. Weltje, M.R. Bloemsa, R. Tjallingii, D. Heslop, and U. Röhl. Prediction of geochemical composition from xrf-corescanner data: A new multivariate approach including filtering, sample selection, and quantification of uncertainties. Accessed: 12.7.2012.

- [9] R. Van Grieken and A. Markowicz. *Handbook of X-Ray Spectrometry, Second Edition*,. Practical Spectroscopy. Taylor & Francis, 2001.
- [10] E.P. Bertin. *Principles and Practice of X-Ray Spectrometric Analysis*. Plenum Press, 1975.
- [11] E. Margui and R. Van Grieken. *X-ray Fluorescence Spectrometry and Related Techniques: An Introduction*. Momentum Press, 2013.
- [12] P. Wobrauschek. personal email conversation: Re: Masterarbeit martin miedler. email: wobi@ati.ac.at. 15.1.2015.
- [13] G. Lutz. *Semiconductor Radiation Detectors*. Accelerator Physics Series. Springer-Verlag, 1999.
- [14] J. Kemmer and G. Lutz. New detector concepts. *Nuclear Instruments and Methods in Physics Research Section A: Accelerators, Spectrometers, Detectors and Associated Equipment*, 253(3):365 – 377, 1987.
- [15] P. Lechner, A. Pahlke, and H. Soltau. Novel high-resolution silicon drift detectors. *X-Ray Spectrometry*, 33(4):256–261, 2004.
- [16] N.A. Dyson. The escape peak in si(li) planar detectors. *Nuclear Instruments and Methods*, 114(1):131 – 133, 1974.
- [17] P J Statham. Escape peaks and internal fluorescence for a si(li) detector and general geometry. *Journal of Physics E: Scientific Instruments*, 9(11):1023, 1976.
- [18] O. Klein and Y. Nishina. Über die streuung von strahlung durch freie elektronen nach der neuen relativistischen quantendynamik von dirac. *Zeitschrift für Physik*, 52(11-12):853–868, 1929.
- [19] B. Andreas, Y. Azuma, G. Bartl, P. Becker, H. Bettin, M. Borys, I. Busch, M. Gray, P. Fuchs, K. Fujii, H. Fujimoto, E. Kessler, M. Krumrey, U. Kuetgens, N. Kuramoto, G. Mana, P. Manson, E. Massa, S. Mizushima, A. Nicolaus, A. Picard, A. Pramann, O. Rienitz, D. Schiel, S. Valkiers, and A. Waseda. Determination of the avogadro constant by counting the atoms in a ^{28}Si crystal. *Phys. Rev. Lett.*, 106:030801, Jan 2011.
- [20] T. Busse. Chapter 12 lecture notes. <http://whs.wsd.wednet.edu/faculty/busse/mathhomepage/busseclasses/radiationphysics/lecturenotes/chapter12/chapter12.html>. Accessed: 12.8.2013.
- [21] Friedrich Herrmann. *Alltasten der Physik*, volume 1. Aulis, 2002.
- [22] S. Flügge. *Encyclopedia of physics*. Handbuch der Physik. Springer-Verlag, 1957.

- [23] A.C. Thompson. *X-ray data booklet*. University of Berkeley, Oct 2009.
- [24] Peter J. Mohr, Barry N. Taylor, and David B. Newell. Codata recommended values of the fundamental physical constants: 2010. *Rev. Mod. Phys.*, 84:1527–1605, Nov 2012.
- [25] Kenjiro Takada. 3-7: The Compton effect. http://www.kutl.kyushu-u.ac.jp/seminar/MicroWorld1_E/Part3_E/P37_E/Compton_effect_E.htm. Accessed: 13.8.2013.
- [26] P. Van Espen. *Spectrum Evaluation*. Handbook of X-Ray Spectrometry, Second Edition,. Marcel Dekker, 2002.
- [27] D. B. Smith. Rhyolite, glass mountain, rgm-1. http://minerals.cr.usgs.gov/geo_chem_stand/rhyolite.html. Accessed: 18.6.2014.
- [28] D. B. Smith. Quartz latite, qlo-1. http://crystal.usgs.gov/geochemical_reference_standards/quartz.html. Accessed: 18.6.2014.
- [29] D. B. Smith. Icelandic basalt, bir-1. http://minerals.cr.usgs.gov/geo_chem_stand/icelandic.pdf. Accessed: 18.6.2014.
- [30] D. B. Smith. Dolerite, dnc-1. http://minerals.cr.usgs.gov/geo_chem_stand/dolerite.pdf. Accessed: 18.6.2014.
- [31] D. B. Smith. Cody shale, sco-1. http://minerals.cr.usgs.gov/geo_chem_stand/codyshale.pdf. Accessed: 18.6.2014.
- [32] D. B. Smith. Mica schist, sdc-1. http://minerals.cr.usgs.gov/geo_chem_stand/mica.pdf. 18.6.2014.
- [33] D. B. Smith. Diabase, w-2. http://minerals.cr.usgs.gov/geo_chem_stand/diabase.html. Accessed: 18.6.2014.
- [34] J. Sherman. The theoretical derivation of fluorescent x-ray intensities from mixtures. *Spectrochimica Acta*, 7:283–306, 1956.
- [35] D.L. Massart. *Handbook of Chemometrics and Qualimetrics*. Number Teil 1 in Data Handling in Science and Technology. Elsevier, 2005.
- [36] George Andermann and J. W. Kemp. Scattered x-rays as internal standards in x-ray emission spectroscopy. *Analytical Chemistry*, 30(8):1306–1309, 1958.
- [37] Röhl U. Tjallingii R., Weltje G. J. Physical parameters and xrf core scanning. XRF core scanning Workshop 2010.

- [38] Rik Tjallingii, Ursula Röhl, Martin Kölling, and Torsten Bickert. Influence of the water content on x-ray fluorescence core-scanning measurements in soft marine sediments. *Geochemistry, Geophysics, Geosystems*, 8(2), 2007.
- [39] J. Aitchison. The statistical analysis of compositional data. *Journal of the Royal Statistical Society*, 44:139–177, 1982.
- [40] J. Aitchison. *The Statistical Analysis of Compositional Data*. Chapman and Hall, 1986.
- [41] Andrew Oddy, Philippa Pearce, and Lorna Green. An unusual gilding technique on some egyptian bronzes. *Conservation of ancient Egyptian materials*, pages 35–9, 1988.
- [42] Tolosana-Delgado R. Pawlowsky-Glahn V., Egozcue J. J. Lecture notes on compositional data analysis. <http://dugi-doc.udg.edu/bitstream/handle/10256/297/CoDa-book.pdf?sequence=1>. Accessed: 28.05.2013.

Repeated measurements with the micro XRF setup

1. To connect the stage with the controller, open “SMC 100 UserTool”
Configuration → comm. Settings → press “open” if not already open.
→ control address setting → press “set”

Motion Portal → tab “Controllers” press “scan” and then “apply”
→ tab “Move” or “Jag” press “home”¹
→ press “*disable*”²
→ press “back” → press “EXIT”
2. To adjust the measuring parameters, open “Newport Canberra controller center”

Newport → Connection... → press “connect”
3. To connect the detector with the program follow the steps:

Canberra → MCA Connect → select “Detector”
→ select “Det-SSD” → press “Ok”
4. To define the amount of repetitions and duration³, follow:

Measurement → Setup XY Movement... → set steps e.g. 1 to 10 for 11 reps.
→ set dwelltime (= measuring time)
→ press “Ok”
5. The next step is to create an outputfile:

Canberra → Save as → choose a filename and press “save”
6. Check if green light on the controller is blinking. If it does, press “run” to start the measurements.

¹The Stage moves to the home position and the light on the controller turns green to indicate that it is now referenced

²The green light on the controller is now blinking, indicating the movement of this controller is disabled

³All other options can be ignored, since the the stage movement is disabled

Line scans with the micro XRF setup

1. To connect the stage with the controller, open “SMC 100 UserTool”

Configuration → comm. Settings → press “open” if not already open.
→ control address setting → press “set”

Motion Portal → tab “Controllers” press “scan” then “apply”
→ tab “Move” or “Jag” press “home”¹
→ press “back” → press “EXIT”

2. To adjust the measuring parameters, open “Newport Canberra controller center”

Newport → Connection... → press “connect”

3. To connect the detector with the program follow the steps:

Canberra → MCA Connect → select “Detector”
→ select “Det-SSD” → press “Ok”

4. To define the starting point, stepsize, amount of steps and measuring time, follow:

Measurement → Setup XY Movement... → set Origin $x = 0$
→ set delta e.g. 0.5
→ set steps e.g. -10 to 10
→ set dwelltime (= measuring time)
→ press “Ok”

5. The next step is to create an outputfile:

Canberra → Save as → choose a filename and press “save”

6. Check if green light of controller is on. If it is, press “run” to start the measurements.

¹The Stage moves to the home position and the light on the control unit turns green to indicate that it is now referenced

Measurements with the hand-held XRF

1. Connect the XRF device with the PC (hand-held device - RS-232 - USB)
2. Open “ViewComPorts” (“ViewComPorts” will indicate the port the device is connected to)
3. Close “ViewComPorts”
4. Open “XRayOps(2)”
5. Fill in “Comm Port #”
6. Checkmark “Open XRay Comm Port” and choose parameters (different presets can be selected aswell)
7. Click “Update Settings” (Parameters can be checked by clicking “Monitor Actuals” and then “PC-Trigger” [x-rays are on then])
8. Uncheck field “Open XRay Comm Port”
9. Open “S1PXRF(2)”, click on the red circle on the upper left corner. (It should turn green)
10. Select “Timed” and then “Timed Assays” to carry out measurement
11. Choose filename and saving folder and applied with “ok”

Function

Import_AXS_Export.m

Input: csv file that contains among other things the recorded spectra

Output: txt .txt-file with the same name as the .csv-file

```
function [Intensity, outfilename] = f_Import_AXS_Export(filename)
%% Import data from text file.
%% Initialize variables.
%filename = 'C:\Users\Martin\Desktop\Brucker AXS Data\originals\
35 kV 2uA Jap Tower 3rd fl leafe green glass 500s.csv';
delimiter = ',';
startRow = 22;
endRow = 1045;

%% Read columns of data as strings:
% For more information, see the TEXTSCAN documentation.
formatSpec = '%*s%s%[\n\r]';

%% Open the text file.
fileID = fopen(filename,'r');

%% Read columns of data according to format string.
% This call is based on the structure of the file used to generate this
% code. If an error occurs for a different file, try regenerating the code
% from the Import Tool.
dataArray = textscan(fileID, formatSpec, endRow-startRow+1, 'Delimiter',
delimiter, 'HeaderLines', startRow-1, 'ReturnOnError', false);

%% Close the text file.
fclose(fileID);

%% Convert the contents of columns containing numeric
```

```

%%strings to numbers.
% Replace non-numeric strings with NaN.
raw = [dataArray{:},1:end-1];
numericData = NaN(size(dataArray{1},1),size(dataArray,2));

% Converts strings in the input cell array to numbers.
%Replaced non-numeric strings with NaN.
rowData = dataArray{1};
for row=1:size(rowData, 1);
    % Create a regular expression to detect and remove
    non-numeric prefixes and
    % suffixes.
    regexstr = '(?<prefix>.*?)(?<numbers>([-]*(\d+[\,]*)+[\.]
{0,1}\d*[eEdD]{0,1}[-+]*\d*[i]{0,1})|([-]*(\d+[\,]*)*[\.]
{1,1}\d+[eEdD]{0,1}[-+]*\d*[i]{0,1}))(?<suffix>.*)';
    try
        result = regexp(rowData{row}, regexstr, 'names');
        numbers = result.numbers;

        % Detected commas in non-thousand locations.
        invalidThousandsSeparator = false;
        if any(numbers==' ');
            thousandsRegExp = '^(\d+?(\,\d{3})*\.\{0,1\}\d*$)';
            if isempty(regexp(thousandsRegExp, ',','once'));
                numbers = NaN;
                invalidThousandsSeparator = true;
            end
        end
        end
    % Convert numeric strings to numbers.
    if ~invalidThousandsSeparator;
        numbers = textscan(strrep(numbers, ',',' '), '%f');
        numericData(row, 1) = numbers{1};
        raw{row, 1} = numbers{1};
    end
    catch me
    end
end

%% Allocate imported array to column variable names
Intensity = cell2mat(raw(:, 1));

%% Clear temporary variables
%clearvars filename delimiter startRow endRow formatSpec

```

```
%fileID dataArray ans raw numericData rawData row regexstr
%result numbers invalidThousandsSeparator thousandsRegExp me;

%%Output filename
basename = strtok(filename, '.');
outfilename = strcat(basename, '.txt');

%%Write text file
dlmwrite(outfilename, Intensity, 'newline', 'pc')
```

Mathematical concepts of compositional data

A mathematical definition of the concepts of composition, simplex, closure, and subcomposition is given by *Pawlowsky-Glahn* in [42]:

Composition: A row vector $\mathbf{x} = [x_1, x_2, \dots, x_D]$, is defined as D -part composition when all its components are *strictly positive real numbers* and they carry only *relative numbers*.

Compositional Data does not apply on the geometrical space \mathbb{R}^D where unconstrained, free data values can vary independently between $-\infty$ and $+\infty$. It has its own sample space, called the *simplex*, which defines all possible combinations a sample with D components can occupy.

Simplex: The D -variate data constrained to a constant sum forms a $D - 1$ dimensional sample space or simplex.

In mathematical terms this is written as:

$$S^D = \{ \mathbf{x} = [x_1, x_2, \dots, x_D] | x_i > 0, i = 1, 2, \dots, D; \sum_{i=1}^D x_i = k \} \quad (1)$$

Closure: For any vector of D real positive components

$$\mathbf{z} = [z_1, z_2, \dots, z_D] \in \mathbb{R}_+^D \quad \text{with} \quad z_i > 0, i = 1, 2, \dots, D$$

the closure of \mathbf{z} is defined as

$$C(\mathbf{z}) = \left[\frac{\kappa \cdot z_1}{\sum_{i=1}^D z_i}, \frac{\kappa \cdot z_2}{\sum_{i=1}^D z_i}, \dots, \frac{\kappa \cdot z_D}{\sum_{i=1}^D z_i} \right] \quad (2)$$

This expression results in a rescaled vector with a sum κ .

Subcomposition: Given a composition \mathbf{x} , a subcomposition \mathbf{x}_s with s parts is obtained by applying the closure operation to a subvector $[x_{i_1}, x_{i_2}, \dots, x_{i_s}]$ of \mathbf{x} . The subindexes i_1, i_2, \dots, i_s refer to the selected parts (not necessarily the first s ones).